Energy landscape and flow dynamics measurements of driven-dissipative systems

Vincent Dumont,[1,*] Markus Bestler,[2] Letizia Catalini,[1] Gabriel Margiani ⬮,[1] Oded Zilberberg,[2] and Alexander Eichler ⬮[1]

[1]*Laboratory for Solid State Physics, ETH Zürich, CH-8093 Zürich, Switzerland*
[2]*Department of Physics, University of Konstanz, D-78457 Konstanz, Germany*

Many experimental techniques aim at determining the energy landscape of a system given and compare it to a model Hamiltonian. This landscape governs the system's evolution in the absence of dissipation. Here, we theoretically propose and experimentally demonstrate a method to measure the energy landscape of a system without knowing its functional form. A crucial ingredient for our method is the presence of dissipation, which enables sampling of the landscape over a large area of phase space through ringdown-type measurements, overcoming the main limitation of previous techniques. We apply the method to a driven-dissipative system–a parametric oscillator–observed in a rotating frame. We first measure the phase-space flow dynamics of the system via ringdown measurements, unveiling its attractors and separatrices. With these measurements, we reconstruct the (quasi-)energy landscape of the system. Furthermore, we demonstrate that our method provides direct experimental access to the so-called symplectic norm of the stationary states of the system, which is tied to the particle- or holelike nature of excitations of these states. In this way, we establish a method to identify qualitative differences between the fluctuations around stabilized minima and maxima of the nonlinear out-of-equilibrium stationary states. Our method constitutes a versatile approach to characterize a wide class of driven-dissipative systems.

I. INTRODUCTION

The evolution of any physical system is governed by an interplay between conservative and nonconservative forces. The former are generated by an energy landscape, i.e., the sum of all energy terms within a closed system. Understanding and controlling an experiment usually requires knowledge of the system's model Hamiltonian. In a realistic setting, however, it can be difficult to compute the Hamiltonian from first principles, as it requires full insight into all microscopic constituents. Alternatively, extracting the effective Hamiltonian from a measurement provides direct access to the system dynamics even when its theoretical model is incomplete. Once the functional form of the Hamiltonian is known, such measurements allow extracting the precise parameters of a system [1]. A prime example is the calibration of qubits, whose gate operations rely on precise Hamiltonian estimations [2–5]. The situation is generally more challenging when the functional form is not known.

Additionally, a vast majority of systems are inherently open, i.e., the dissipative coupling to an environment cannot be ignored. An open system experiences fluctuations that cause it to sample the available landscape over time. This allows estimating a system's Hamiltonian by measuring the probability of finding it in a certain state while it is subject to fluctuations [6–13]. This method was used in experimental studies of the escape dynamics [13] and Kramers turnover [11] of a particle trapped in an optical potential, investigations of the force fields acting on these particles [14,15], or the stability of coupled nonlinear systems [16,17]. Probabilistic methods have the drawback that certain states are rarely explored. As such, these methods are often inadequate in situations where regions of interest (in phase space) are separated by large energy differences. In addition, these methods are insensitive to temporal correlations in the system, which pertain to the notion of causality of excitations, as quantified by, e.g., out-of-time-ordered correlators [18,19].

In the presence of dissipative coupling to an environment, it is also possible to probe a system's Hamiltonian from its deterministic relaxation. This becomes feasible when the measured variables of interest are large enough to neglect the impact of fluctuations. By initializing a system in a well-defined state using an external drive and then turning off the drive, the system decays into a stationary state due to dissipative coupling to a large and, most often, Markovian reservoir. By measuring such a ringdown into a stationary state (attractor), both the nonlinearity of a system close to a stable solution [20–23] and the curvature of engineered energy landscapes [24] have been measured in the absence of a drive.

In principle, such ringdown-type experiments can be extended to driven-dissipative systems. This is particularly interesting for driven nonlinear systems with multiple stable oscillation states. In a rotating frame, such oscillations can appear as stationary states within their respective basins of attraction [25,26]. There, the system dynamics can be described by a rotating-frame quasi-Hamiltonian that, for instance, allows understanding out-of-equilibrium phase transitions [27–31] in lattices of cold atoms [24], optical

---

oscillators [32], or cavity magnonic systems [33]. Interestingly, such systems can stabilize out-of-equilibrium phases where seemingly anticausal excitations can manifest [29,34]. However, to our knowledge, no full reconstruction of such a rotating-frame energy landscape has been reported to date.

In this paper, we demonstrate a deterministic method for qualitatively reconstructing the full rotating-frame flow dynamics and quasi-Hamiltonian of a driven-dissipative nonlinear system using systematic ringdown measurements. Notably, the presence of dissipation enables sampling of a large section of a Hamiltonian from a limited number of ringdown measurements. The method we demonstrate here can be used to reconstruct the flow dynamics and energy landscape of systems with unknown functional form, and in the presence of damping. This is in contrast to typical Hamiltonian learning algorithms in quantum systems that aim at estimating very precisely the coefficients of a known or supposed Hamiltonian model, e.g., coupled qubits [35–37]. Our method provides high resolution even far from stationary solutions, where stochastic approaches typically fail. Furthermore, our method yields a picture of the phase-space flow dynamics, steady-state solutions, and separatrices of the system. We obtain a direct measurement of the symplectic norm of each solution [29,30], providing a qualitative understanding of the different phases the system can enter, including a dissipation-stabilized maximum with hole-like quasiparticle excitations. Importantly, our method can be extended and applied to both undriven and driven-dissipative oscillating systems far from equilibrium, making it a valuable tool in many contemporary fields of physics.

We first present in Sec. II our electromechanical resonator system. In Sec. III, we introduce the general method to reconstruct the Hamiltonian from ringdown measurements. In Sec. IV, we reconstruct the effective Hamiltonian of our resonator in the absence of a drive, i.e., demonstrating the method for a standard damped harmonic oscillator. Then, in Sec. V, we subject the resonator to a large parametric drive to allow multiple stable oscillation solutions, and measure its phase-space flow dynamics. With this measurement, we extract the rotating-frame quasienergy and compare it to theoretical predictions. Finally, in Sec. VI, we discuss the extraction and implications of the symplectic norm as a tool for exploring and understanding out-of-equilibrium stationary solutions.

II. ELECTROMECHANICAL DEVICE

Our device is a micro-electromechanical resonator, as illustrated in Fig. 1(a). It consists of a mechanical cantilever [38] biased with voltage $U_{bias} \approx 32$ V, used to tune the mechanical resonance frequency ω_0 [39], and which induces a Duffing nonlinearity β (due to the non-linearity of the electrostatic force between the mechanical element and the electrodes [38]). To generate a weak near-resonant forcing term F, we apply a voltage $\tilde{U}_r = U_r \cos(\omega_r t + \theta)$ to one of the electrodes, where U_r is the amplitude, θ is a phase offset, and $\omega_r \approx \omega_0$. A large off-resonant voltage $\tilde{U}_p = U_p \cos(2\omega_r t + \psi)$ periodically modulates ω_0 with a modulation depth $\lambda \propto U_p$, making it possible to parametrically drive the resonator [40]. We read out the mechanical displacement x via the output voltage $U_{out} \propto x$ with a lock-in amplifier (Zurich Instruments
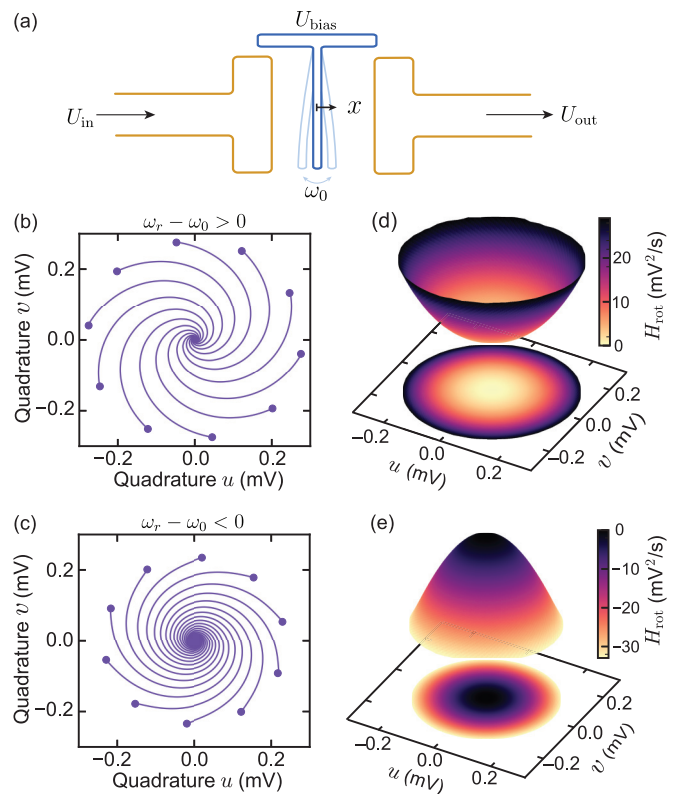

FIG. 1. Microelectromechanical resonator and H_{rot} reconstruction of a simple damped harmonic oscillator from ringdown measurements. (a) A cantilever, biased at voltage U_{bias}, with oscillation displacement x and natural frequency ω_0, is capacitively coupled to two conductors. Typically, an input voltage $U_{in} = \tilde{U}_r + \tilde{U}_p$ with frequency ω_r ($2\omega_r$) can drive the mechanical resonator resonantly (parametrically), when $\omega_r \approx \omega_0$. The mechanical motion induces a voltage U_{out}, which we read out. (b) Several ringdown measurements for a few initialization points (dots) in rotating (i.e., at demodulated frequency ω_r) phase space (u, v) for blue detuned demodulation, $(\omega_r - \omega_0)/2\pi \approx 91$ Hz. The point-to-point error is too small to be visible. (c) Several ringdown measurements in phase space for red detuned demodulation, $(\omega_r - \omega_0)/2\pi \approx -209$ Hz. (d) Reconstructed Hamiltonian for positive detuning, i.e., from measurements of (b), using Eq. (5), shown in three dimensions and as a two-dimensional colorplot. (e) Reconstructed Hamiltonian for negative detuning, i.e., from the measurements of panel (c).

MFLI), and ignore the proportionality coefficient for convenience (i.e., we define $U_{out} \equiv x$) [41]. The device displacement is described by the equation of motion (EOM)

$$\frac{d^2x}{dt^2} + \omega_0^2[1 - \lambda \cos(2\omega_r t + \psi)]x + \Gamma\frac{dx}{dt} + \beta x^3 = F, \quad (1)$$

with time t. The device has a mechanical resonance frequency $\omega_0/2\pi \approx 1.12$ MHz, energy decay rate $\Gamma/2\pi \approx 112$ Hz (quality factor $Q = \omega_0/\Gamma \approx 10^4$), and Duffing nonlinearity $\beta \approx -9.9 \times 10^{-16}$ V^{-2}s^{-2}. The forcing term (in units of Vs^{-2}) is $F = A\tilde{U}_r$ with a conversion factor $A \approx 16 \times 10^6$ s^{-2} and with the oscillator's mass absorbed in the definition of F. The parametric drive voltage amplitude U_p can be converted to a parametric modulation depth $\lambda = 2U_p/QU_{th}$ by measuring the parametric drive threshold amplitude $U_{th} \approx$

1.98 V. Above the parametric threshold, the system can be driven into an out-of-equilibrium stationary oscillation via a spontaneous time-translation symmetry breaking [4,8,40,42–50]. The full device characterization is shown in Appendix A.

III. HAMILTONIAN RECONSTRUCTION

We now introduce our method for reconstructing the Hamiltonian from measured coordinates along a trajectory. The evolution of a classical lossless system in the laboratory frame with coordinate x and its conjugate p is given by Hamilton's EOMs

$$\frac{dx}{dt} = +\frac{\partial H(x, p)}{\partial p}, \quad \frac{dp}{dt} = -\frac{\partial H(x, p)}{\partial x}, \quad (2)$$

where $H(x, p)$ is the Hamiltonian. Here, for any initial conditions and without drive, trajectories form closed loops along energy contour lines in coordinate space (x, p) since there is no energy loss. This means that only a single energy contour of the Hamiltonian can be sampled when following any given trajectory. To sample all energy elevations, one has to initialize the system at infinitely many different initial conditions.

In many cases, we are interested in the slowly varying in-phase and out-of-phase quadratures $u(t)$ and $v(t)$ observed in a frame rotating at $\omega_r \approx \omega_0$, which are defined via $x(t) = u(t)\cos(\omega_r t) - v(t)\sin(\omega_r t)$. The demodulated quadrature we measure with our lock-in amplifier at frequency ω_r are precisely u and v. By applying the averaging method [51] on an equation of motion such as Eq. (1), we obtain the so-called slow-flow equations (see Appendix B). We open the system by adding dissipative terms $\propto \Gamma$, i.e., we consider rotating Lagrangian dynamics, such that the equations of motion can be formulated in a similar structure as Eq. (2):

$$\frac{du}{dt} = +\frac{\partial H_{\mathrm{rot}}(u, v)}{\partial v} - \frac{\Gamma}{2}u,$$
$$\frac{dv}{dt} = -\frac{\partial H_{\mathrm{rot}}(u, v)}{\partial u} - \frac{\Gamma}{2}v. \quad (3)$$

In this frame, the energy-conserving evolution of the system is governed by a rotating-frame quasi-Hamiltonian H_{rot}. For our resonator, subjected to both parametric and external drives, H_{rot} reads [52]

$$H_{\mathrm{rot}} = \frac{\omega_r^2 - \omega_0^2}{4\omega_r}(u^2 + v^2)$$
$$- \frac{3\beta}{32\omega_r}(2u^2v^2 + u^4 + v^4)$$
$$+ \frac{\lambda\omega_0^2}{8\omega_r}(2uv\sin\psi + (u^2 - v^2)\cos\psi)$$
$$+ \frac{AU_r}{2\omega_r}(u\cos\theta + v\sin\theta). \quad (4)$$

This Hamiltonian H_{rot} is a function in the rotating phase space spanned by u and v [20], and is the quantity we reconstruct in this paper.

The addition of dissipation in Eq. (3) is crucial. On the one hand, in the presence of dissipation, a trajectory is no longer confined to a single closed loop, but samples different energy contours. On the other hand, dissipation causes the

system to converge towards one of the stable stationary states of the system, see Fig. 1(b). This allows us to probe H_{rot} by experimentally measuring $u(t)$ and $v(t)$ using rotating-frame ringdown measurements. By initializing the system in an initial state (u_i, v_i) and letting it evolve to a final state (u_f, v_f), we can extract the change in the Hamiltonian ΔH_{rot} at any point (u_j, v_j) along this ringdown's trajectory. We isolate H_{rot} in Eq. (3) and integrate over the slow coordinates from (u_i, v_i) to (u_j, v_j) to obtain

$$\Delta H_{\mathrm{rot}} = \int_{v_i}^{v_j}\left[\frac{du}{dt} + \frac{\Gamma}{2}u\right]dv - \int_{u_i}^{u_j}\left[\frac{dv}{dt} + \frac{\Gamma}{2}v\right]du. \quad (5)$$

In practice, the values (u_j, v_j) are measured in discrete steps, allowing us to compute ΔH_{rot} only at these points. Measuring multiple ringdowns with different initial (u_i, v_i), ΔH_{rot} can be deterministically sampled and reconstructed over a large area of phase space, with a resolution limited by the measurement uncertainty or fluctuations (e.g., thermal or quantum noise) in u and v. Note that Eq. (5) does not provide the relative change of ΔH_{rot} between different ringdown measurements.

To compare different traces, we make use of the fact that $H_{\mathrm{rot}}(u_f, v_f)$ should be single-valued at stationary points. This means that all traces sharing the same final coordinates (u_f, v_f) should have the same final value $H_{\mathrm{rot}}(u_f, v_f)$. We thus find the relative Hamiltonian offset between different ringdown traces sharing the same (u_f, v_f) by comparing $H_{\mathrm{rot}}(u_f, v_f)$. Finding the offset between traces is more complicated when they have different values of (u_f, v_f), i.e., they do not share a common end point. Here, the offset can be calculated by making the Hamiltonian continuous, i.e., by finding the offset that minimizes the difference between nearby starting points (u_i, v_i) that decay into different final (u_f, v_f), see Appendix C.

We emphasize that our method can reconstruct a Hamiltonian without assuming its functional form. In other words, it allows us to measure the energy landscape of an arbitrary system. The main assumption is that the impact of noise is small, see Appendix D, and that we know the form and magnitude of the dissipation. The dissipation coefficient Γ can be measured in a standard ringdown experiment, from which we can also confirm the absence of nonlinear damping [23,53,54], cf. Appendix A. Importantly, if nonlinear damping was measured in the ringdown experiment, the EOMs [Eq. (3)] can be modified to include it, and our method will still work. Note also that a Hamiltonian reconstruction analogous to Eq. (5) can also be performed in the nonrotating frame, i.e., for a dissipative Eq. (2). We concentrate here on the case of a rotating-frame Hamiltonian to be in line with the theory. In the following, we will test the Hamiltonian reconstruction before discussing what information we can extract from it.

IV. HARMONIC OSCILLATOR CASE

As a first demonstration, we reconstruct the rotating-frame Hamiltonian of a damped harmonic oscillator. In Figs. 1(b) and 1(c), we show multiple measured trajectories for the case $\lambda = 0$, and with amplitudes that are small enough to neglect the effect of the Duffing non-linearity, i.e., only considering the first line in Eq. (4). For each of those ringdown trajectories, we first displace the resonator in phase space using a

near-resonant drive with fixed U_r and ω_r, and with an individually selected θ. In a frame rotating at ω_r, the corresponding initial resonator coordinates (u_i, v_i), shown as dots, are stationary under the resonant drive. Then, we switch off the drive ($U_r = F = 0$), and track the ringdown trajectory while the system decays to the state ($u_f = 0, v_f = 0$). We measure the demodulated signal with a sampling rate 54 kHz $\gg \Gamma$ in order to resolve the ringdowns [55]. During this decay, the angle of the state in phase space evolves in time since the rotating frame's frequency is detuned from the resonance frequency [21]. For $\omega_r - \omega_0 > 0$ in Fig. 1(b), the trajectories spiral towards $(0, 0)$ with a clockwise orientation, while for $\omega_r - \omega_0 < 0$ in Fig. 1(c), they spiral in the counterclockwise direction. The chirality of the ringdown trajectory therefore shows whether the oscillator moves with a lower or higher frequency than ω_r near the stable state. Note that the choice of the rotating frame impacts the chirality of the ringdowns and associated effects.

We reconstruct the energy landscape, i.e., the rotating-frame Hamiltonian H_{rot}, from the ringdown trajectories using Eq. (5). For the reconstructions in Figs. 1(d) and 1(e), the resolution was improved by using more ringdown traces than shown in Figs. 1(b) and 1(c). The residuals of these two reconstructions are shown in Appendix E. The resulting H_{rot} is a paraboloid whose sign of curvature depends on $\omega_r - \omega_0$. This is predicted in Eq. (4) and reflects the fact that H_{rot} describes energy relative to a rotating frame. Indeed, for $\omega_r - \omega_0 = 0$, the rotating energy landscape would be entirely flat. Note that the origin $(0, 0)$, which appears as a maximum of H_{rot} in Fig. 1(e), remains the only stable solution of the system irrespective of the detuning. As a (local) maximum can appear as a stationary state, this example demonstrates that the rotating-frame Hamiltonian cannot be interpreted as a simple energy function as is the case in the nonrotating frame [51]. After successfully reconstructing the rotating frame energy of a harmonic oscillator, we now apply our method to a more complex system.

V. PARAMETRIC OSCILLATOR CASE

The reconstruction of H_{rot} can also be applied to driven nonlinear systems with multiple stable solutions. Here, we demonstrate this principle on the example of the electromechanical resonator described in Sec. II when subjected to a parametric drive, cf. Eq. (4) and Fig. 1(a).

We first analyze a single rotating-frame ringdown into an out-of-equilibrium stationary state in phase space. In Fig. 2, we study an example trajectory of our system in the presence of parametric driving beyond the instability threshold ($\lambda > \lambda_{th}$) [51], where two time-translation symmetry-broken high-amplitude solutions are stabilized due to the interplay between the drive and the nonlinearity, see Appendix A. As shown schematically in Fig. 2(a), the system is initialized in (u_i, v_i) by a near-resonant force at ω_r, followed by a parametric drive tone whose amplitude $\lambda \propto U_p$ and frequency $2\omega_r$ define the stationary solutions of the system in the readout frame rotating at frequency ω_r [51,56,57]. In Fig. 2(b), we show a typical ringdown trajectory of our resonator in phase space, noting that ($u_f \neq 0, v_f \neq 0$).
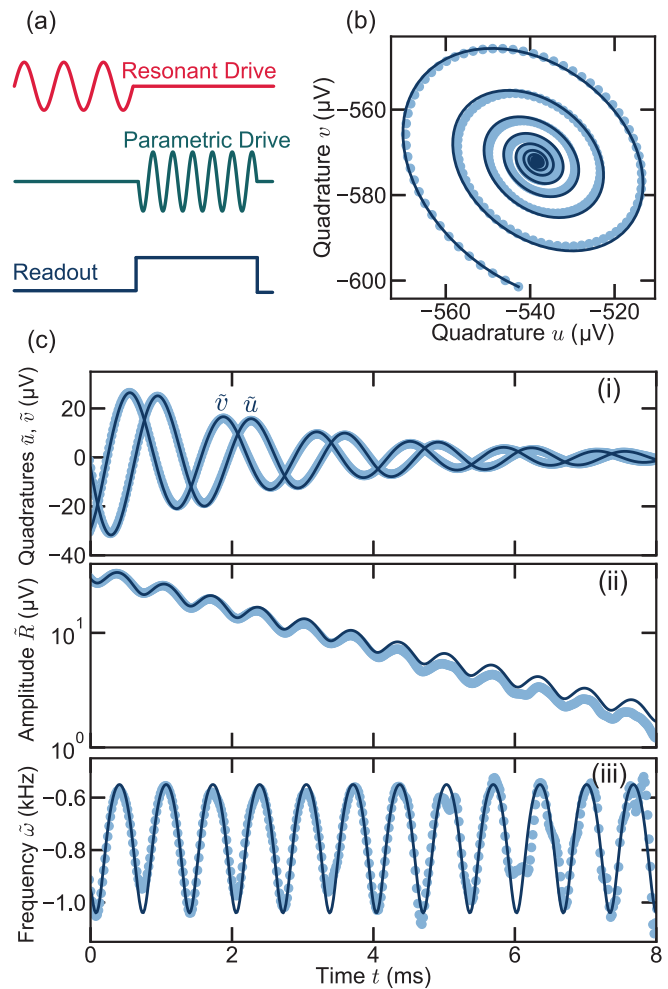

FIG. 2. Ringdown of a parametric oscillator. (a) For a ringdown measurement, the resonator is first displaced with a near-resonant drive $U_{in}(\omega_r)$ with $\omega_r \approx \omega_0$. This resonant drive is turned off and a parametric drive $U_{in}(2\omega_r)$ is immediately turned on, while the slowly varying (i.e., demodulated at ω_r) quadratures u and v are read out. (b) Ringdown in phase space for fixed parametric drive $U_p = 10$ V ($\lambda \approx 10^{-3}$) and frequency $(\omega_r - \omega_0)/2\pi \approx -253$ Hz. The dark blue curve is the predicted ringdown with the linearized model in Appendix B [Eq. (B6)]. (c) In (i) the in-phase $\tilde{u}$ and out-of-phase $\tilde{v}$ displaced quadratures, (ii) amplitude $\tilde{R} = \sqrt{\tilde{u}^2 + \tilde{v}^2}$, and (iii) instantaneous rotating-frame frequency $\tilde{\omega} = \partial_t \tilde{\phi}/2\pi$ with phase $\tilde{\phi} = \arctan(\tilde{v}/\tilde{u})$ are plotted as a function of time for the same ringdown as in (b). These measurements are referenced to the attractor in which they ringdown into, i.e., $\tilde{u} \equiv u - u_f$ with $u_f \approx -538$ μV the final value of u (the position of the attractor), and similarly for $\tilde{v}$ with $v_f \approx -572$ μV.

To facilitate the Hamiltonian reconstruction, we define displaced quadratures $\tilde{u} \equiv u - u_f$ and $\tilde{v} \equiv v - v_f$, with the final coordinates of the ringdown (u_f, v_f) (i.e., the attractor position). In this shifted reference frame, the relaxation into the stable solution resembles a ringdown process in an equilibrium system, with $\tilde{u}$ and $\tilde{v}$ performing damped oscillations towards a final state $(\tilde{u}_f = 0, \tilde{v}_f = 0)$, see Fig. 2(c)(i). The damping rate associated with these trajectories is quantified by the same Γ as we introduced in Eq. (1), while the rotation around (u_f, v_f) depends on H_{rot}. The

dynamics of these shifted quadratures are well captured by linearizing the equations of motion [Eq. (3)] around the attractors, see derivation in Appendix B.

In contrast to undriven relaxation processes in the laboratory frame (x, p), the amplitude $\tilde{R} = \sqrt{\tilde{u}^2 + \tilde{v}^2}$ does not decay monotonically. Instead, we observe oscillations imposed on top of the exponential decay in Fig. 2(c)(ii). These oscillations stem from the fact that the shape of $H_{\rm rot}$ around $(u_{\rm f}, v_{\rm f})$ is not rotationally symmetric, such that the system samples different $\partial_u H_{\rm rot}$ and $\partial_v H_{\rm rot}$ as it moves around the Hamiltonian landscape. We emphasize that despite the fact that we observe oscillations growing in amplitude at certain times, this does not violate any law of conservation, as we are dealing with a driven system. The nonrotationally symmetric Hamiltonian also manifests in Fig. 2(c)(iii), where an instantaneous rotating-frame frequency $\tilde{\omega} = \partial_t \tilde{\phi}/2\pi$ is defined by the phase $\tilde{\phi} = \arctan(\tilde{v}/\tilde{u})$ relative to the attractor.

There are clear oscillations in the frequency $\tilde{\omega}$ due to the resonator sampling different $\partial_u H_{\rm rot}$ and $\partial_v H_{\rm rot}$ as it moves in phase space. This behavior is also well captured by the averaged and linearized dynamics near the attractors (cf. Eq. (3) and Appendix B). Note that for smaller parametric drives or for dynamics further away from the attractors, one needs to consider a model that goes beyond the linearization we employ (i.e., expand the equations to higher-order terms) to fully capture the dynamics.

In a next step, we measure multiple trajectories with various initialization conditions, but fixed parametric drive strength and frequency, allowing us to reconstruct the rotating frame Hamiltonian $H_{\rm rot}$ of our driven nonlinear system. In Fig. 3(a), we show such sets of trajectories for three different parametric drives: (i) below threshold with a single squeezed state, (ii) above threshold with two stable phase states, and (iii) at large driving and large detuning with a combination of phase states and a zero-amplitude state (see Appendix A for a phase diagram of the device). Each ringdown is color-coded by the state it eventually approaches, allowing us to identify the corresponding attractor pools. From ringdown measurements, we can thus directly identify the number of stable solutions in the given phase-space area, as well as the separatrices of the system—the regions where the color of nearby ringdown measurements changes. In addition, we obtain a visualization of the stream flow in phase space, as governed by Eq. (3). We stress that the main assumption of this reconstruction is that the damping is linear, cf. Eqs. (3), though these equations could be adapted to include other types of damping. The reconstruction does not assume linearized dynamics.

The reconstructed Hamiltonians $H_{\rm rot}$ are shown in Fig. 3(b) alongside theoretical Hamiltonians in Fig. 3(c), as calculated from Eq. (4) using parameters ω_0, β, and λ extracted from independent calibration measurements in Appendix A. We find excellent qualitative agreement between measurement and theory, see Appendix E for the residuals, with typical deviations $<10\%$. We stress that only the parametric drive phase ψ is a fit parameter. In Appendix D, we also show the residuals when all the parameters are fitted, showing deviations of a few percents, and discuss the effect of noise on the reconstruction. Crucially, the quality and resolution of the Hamiltonian reconstruction is consistently high over the entire

sampled phase space, which would be hard to achieve with statistical methods [6–13]. In the reconstructed $H_{\rm rot}$, we can clearly see the appearance of one, two, and three stable states in the three cases (i)–(iii), respectively, indicating different phases of the driven system [27,28,58]. Our reconstruction method confirms the theoretical prediction that the stationary solutions can qualitatively differ in the rotating frame; while the phase states at finite amplitude in the cases (ii) and (iii) are marked by a minimum in $H_{\rm rot}$, the stable state appearing at $(u = 0, v = 0)$ in (iii) corresponds to a maximum, signaling a fundamentally different type of solution, i.e., a dissipation-stabilized state [29,30]. In the following, we analyze this difference using the symplectic norm of the individual solutions, and we show that this quantity yields valuable insights into the behavior of driven-dissipative systems.

VI. SYMPLECTIC NORM

In Secs. IV and V, we successfully reconstructed rotating-frame Hamiltonians $H_{\rm rot}$ using ringdown measurements. One of the most prominent distinctions of a rotating-frame Hamiltonian, compared with a Hamiltonian in a laboratory frame such as in Eq. (2), is that both maxima and minima of $H_{\rm rot}$ can constitute stable oscillation states of the system, unlike what we expect from the minimal action principle in equilibrium systems. This counterintuitive feature can be clearly observed in row (iii) of Fig. 3, where two minima at finite amplitudes are separated by a stable local maximum at $(u = v = 0)$. Importantly, the minima in Fig. 3 are stable due to the nonlinearity β, while the maximum is stabilized by dissipation [30]. This fundamental difference, however, is difficult to quantify in standard measurements, such as frequency sweeps and stability diagrams [44,59].

A method tailored to classify and distinguish minima and maxima in $H_{\rm rot}$ is the symplectic norm ds^2 [29,30]. When an excitation is created on top of a stationary state with a negative (positive) symplectic norm, it reduces (increases) the energy of the system relative to the rotating frame, that is, relative to an excitation at the driving frequency $\omega_{\rm r}$. Similar to how the Dirac scalar quantifies particles and holes in relativistic quantum theory [60], the symplectic norm quantifies whether a Bogoliubov excitation in the rotating frame is more particle- or holelike. This difference manifests in the Hamiltonian: stationary solutions with a negative (positive) symplectic norm appear as maxima (minima) in $H_{\rm rot}$ and are formally associated with a holelike (particlelike) excitation, see Appendix B. We can therefore use the reconstructed Hamiltonians in Fig. 3 to directly determine the symplectic norm of the stable oscillations states, and to classify the corresponding excitations.

A careful study of Fig. 3 reveals additional information. Namely, the trajectories leading to Hamiltonian extrema assume clockwise or counterclockwise rotations. We show in Appendix B that for a wide class of systems, the symplectic norm is directly linked to the sense of rotation of the trajectories close to an attractor: an excitation behaves hole- (particle-) like in the rotating frame if it moves slower (faster) than the rotating frame and hence backward (forward) in time relative to the clock given by the rotating frame. The notion of hole- and particlelike excitations is therefore always relative to the rotating frame.
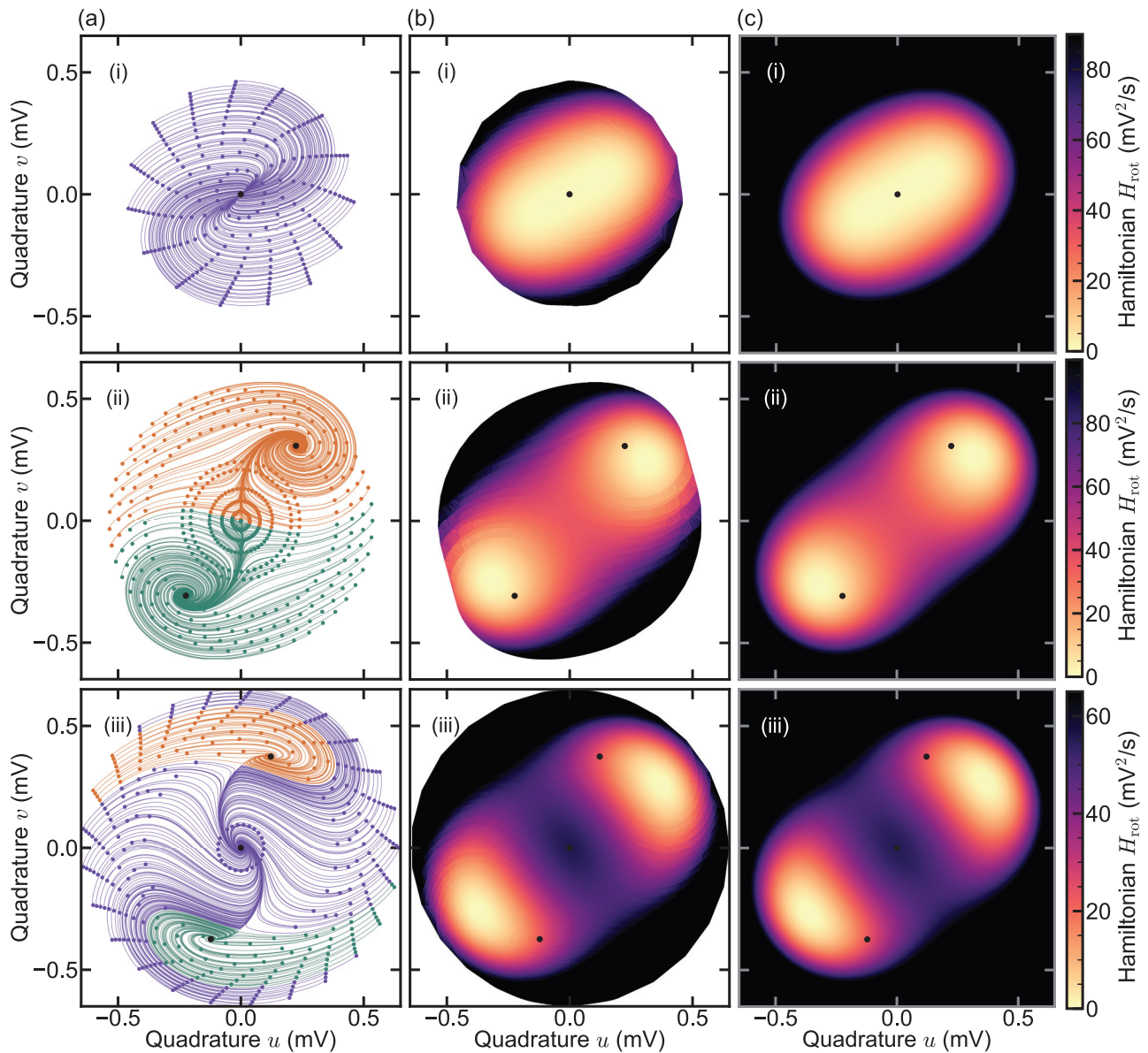
FIG. 3. Ringdown measurements and Hamiltonian reconstruction in parametric phase space. (a) Multiple ringdown measurements in phase space under different parametric drive strength and frequency. Each ringdown's starting point is indicated by a dot, and color-coded for the attractor in which it rings down: purple the zero-amplitude, orange the top-right, and green the bottom-left attractor. The attractors extracted from the ringdown measurements are indicated by black dots. The parametric drive is (i) below threshold, (ii) above threshold, and (iii) above threshold and far detuned, cf. Appendix A for the locations of the measurements relative to the device's phase diagram. (b) Rotating-frame Hamiltonian reconstruction from the ringdown measurements in (a), cf. Eq. (5). (c) Theoretical plots of the rotating-frame Hamiltonian [Eq. (4)] using angle (i) $\psi \approx -2.1$ rad, (ii) $\psi \approx -1.76$ rad, and (iii) $\psi \approx -1.86$ rad as the only fit parameter, while fixing the independently measured mechanical parameters, see Appendix A. Note that the attractors are not necessarily at the minima of the quasi-Hamiltonian due to dissipation [20].

We use the chirality of the rotations to extract the symplectic norm ds^2 of the different attractors directly from the measured ringdown trajectories, without a full reconstruction. To capture this observation mathematically, we define a correlator characterizing the direction of rotation of a ringdown,

$$G^c(t' - t) = \Theta(t' - t)\langle \tilde{v}(t)\tilde{u}(t') - \tilde{u}(t)\tilde{v}(t') \rangle_t, \quad (6)$$

with the Heaviside step function $\Theta(t - t')$, and $\langle ... \rangle_t$ indicating an average over all times t. This quantity $G^c(t - t')$

is a classical analog to the quantum Green's function used in Refs. [30,34,61]. Following these works, we calculate the corresponding spectral response $\mathcal{A}$ of a stable oscillation state

$$\mathcal{A}(\omega) = -2\text{Im}[G^c(\omega)]$$

$$= \frac{|\zeta|^2 ds^2}{2}\left[\frac{1}{(\omega - \omega_{\text{lin}})^2 + \frac{\Gamma^2}{4}} - \frac{1}{(\omega + \omega_{\text{lin}})^2 + \frac{\Gamma^2}{4}} \right],$$
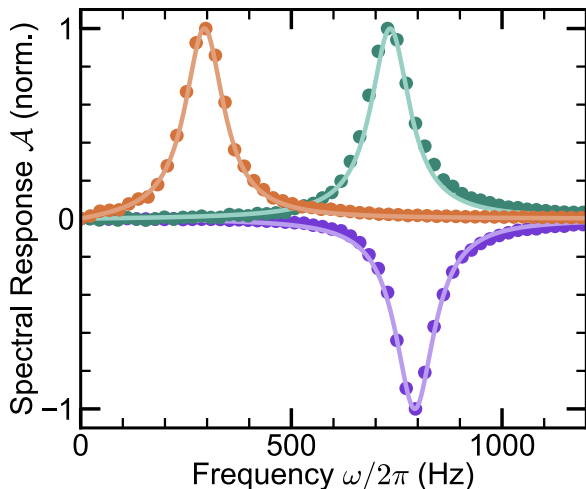
$$(7)$$

FIG. 4. Spectral response of a parametric oscillator. With $\tilde{u}$ and $\tilde{v}$ obtained during a ringdown measurement, we can extract the spectral response $\mathcal{A}$ using Eqs. (6) and (7) (dots) [cf. Figs. (2) and (3)]. These spectral responses are in good agreement with the fitted theoretical curves of Eq. (7), with ω_0 left as a free parameter to account for small frequency drifts. All measurements are done with the same parametric drive strength $U_p = 10$ V ($\lambda \approx 10^{-4}$), and different demodulation frequencies ω_r. The detuning is $(\omega_r - \omega_0)/2\pi \approx 170$ Hz (orange) and $(\omega_r - \omega_0)/2\pi \approx -222$ Hz (green) for ringdowns into high amplitude states, and $(\omega_r - \omega_0)/2\pi \approx -865$ Hz (purple) for the zero amplitude state.

where $G^c(\omega)$ is the Fourier transform of $G^c(t - t')$, ζ is a constant related to the ringdown starting conditions, and ω_{lin} is the oscillation frequency of the quadratures. The linear response function in the second line is only valid near the attractor of interest.

Looking at $\mathcal{A}$, we see that the spectral response has peaks at $\pm\omega_{lin}$, with width Γ, and an overall sign which is determined by the symplectic norm ds^2. Therefore, if the resonator rings down with a counterclockwise (clockwise) rotation in phase space, the final steady state of the system has a negative (positive) symplectic norm and a negative (positive) peak in $\mathcal{A}$.

With this knowledge, we can extract the sign of ds^2 from the spectral response of ringdown measurements, as shown in Fig. 4. We record $\tilde{u}$ and $\tilde{v}$ during one trajectory, calculate the correlator $G^c(t - t')$ [Eq. (6)], take its Fourier transform, and compute the spectral response $\mathcal{A}$ according to Eq. (7). In Fig. 4, we present the measured result for each of the three stable states of a parametric oscillator at different detunings. We compare these measured spectral responses with those expected from theory, calculated using independently measured parameters and the linearized slow-flow equations [Eq. (7)], and obtain very good agreement. As expected, for a stable solution corresponding to a maximum in H_{rot} (purple curve), the spectral response is a dip, while the two other solutions, which are minima in H_{rot} (orange and green curves), correspond to peaks in the spectral response. These measurements show the link between the orientation of rotation, the symplectic norm, the spectral function, and the rotating frame Hamiltonian H_{rot}.

We emphasize that the notion of maxima and minima of the rotating quasienergy depend on the chosen rotating frame

frequency, and that stabilized maxima are a manifestation of out-of-equilibrium stationary states. The classification of the different stationary states can for example be harnessed to find a topological classification of driven-dissipative systems [62].

VII. OUTLOOK

We report a precise method to reconstruct the Hamiltonian of a system via ringdown measurements. The method allows for a full characterization of the energy landscape, including multiple stable solutions, saddle points, and attractor pools. The method is particularly suited for studies in the growing field of driven-dissipative nonlinear systems, where a Hamiltonian characterization from first principles is often very difficult. Furthermore, it bestows the ability to characterize the symplectic norm of different stable oscillation solutions in the rotating frame with a connection to relativistic quantum mechanics and causality. We expect that this approach will allow the classification of a broad variety of systems, including nanomechanics, superconducting circuits, light-matter systems, and nonlinear optics.

ACKNOWLEDGMENTS

APPENDIX A: EXPERIMENTAL CHARACTERIZATION

In this Appendix, we characterize the resonator with various measurements. We first perform parametric sweeps in Sec. A 1 and extract the resonator energy decay rate $\Gamma/2\pi = 112(2)$ Hz, resonance frequency $\omega_0/2\pi = 1.1198294(3)$ MHz, Duffing nonlinearity $\beta = -9.894(4) \times 10^{16}$ (V · s)$^{-2}$, and parametric drive conversion factor $C = 9.88(5) \times 10^3$ V. In Sec. A 2, we perform a resonant drive sweep to extract the factor $A = 16.22(1) \times 10^6$ s^{-2} converting from resonant applied voltage to force. Finally, in Sec. A 3, we perform ringdown measurements showing that the resonator experiences linear damping.

1. Parametric sweeps

In this section, we describe how we measure the parametric response of our resonator in order to extract its resonance frequency ω_0, energy decay rate Γ, and Duffing nonlinearity β.

We send a parametric tone $\tilde{U}_p = U_p \cos(2\omega_r t)$ to our device and read out the induced displacement at frequency ω_r. In Fig. 5(a), we show the system's response while sweeping the frequency of the parametric drive from high to low frequencies for fixed parametric drive voltage $U_p = 4.54$ V. By
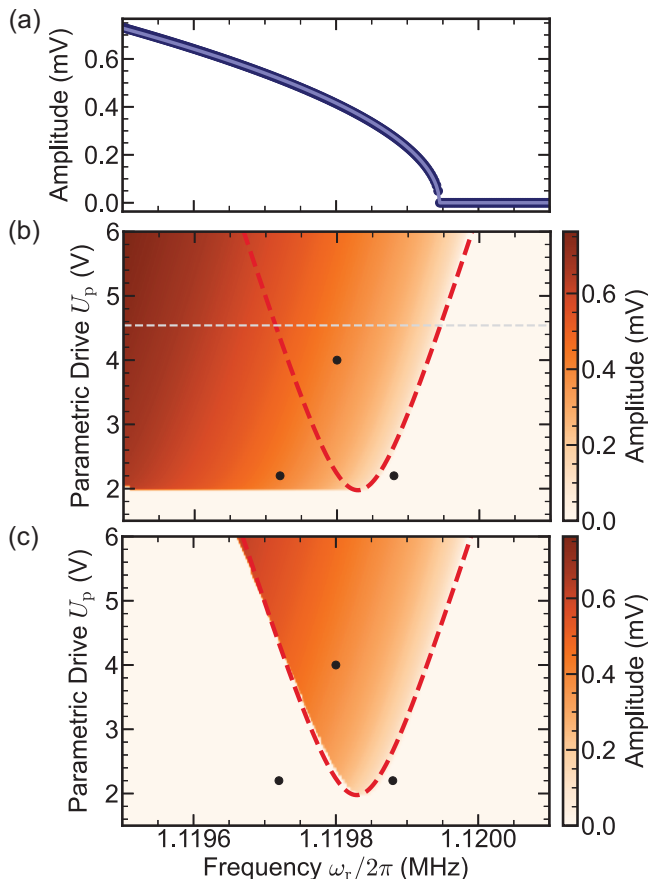
FIG. 5. Parametric response. (a) Measured response of our resonator to a parametric drive $\tilde{U}_\mathrm{p} = U_\mathrm{p} \cos(2\omega_\mathrm{r} t)$ with voltage amplitude $U_\mathrm{p} = 4.54\,\mathrm{V}$. The frequency is swept from high to low values. (b) Response to a parametric drive as in (a) for different values of U_p. The dashed grey line indicates the measurement of (a), the red dashed line corresponds to the fitted Arnold tongue outline [see (c)], while the dots indicate the parameters used in Fig. 3. (c) Response to a parametric drive as in (a) for different values of U_p when sweeping from low to high frequencies.

repeating this measurement for different parametric drive voltages, we obtain the phase diagram of our parametric oscillator, shown in Fig. 5(b). Now, performing the same measurement but instead sweeping the frequency from low to high frequencies (i.e., "against" the Duffing nonlinearity), we obtain a different diagram commonly referred to as Arnold Tongue, shown in Fig. 5(c).

Comparing with theoretical predictions [51], Figs. 5(b) and 5(c) allow us to read out the different phases and number of solutions of our resonator depending on the parametric drive strength and frequency. Indeed, the outline of the Arnold tongue, shown as a red dashed line, indicates the (frequency-dependent) parametric threshold, above which the resonator has exactly two stable states (the parametric phase states), both of which have finite-amplitude but opposite phases. The orange region outside the Arnold tongue in Fig. 5(b) features a zero-amplitude state in addition to the two parametric phase states. Which state is selected depends on the initial condition of the resonator. Finally, in the white region in Fig. 5(b) only the zero-amplitude state is stable.

To find the equation predicting the parametric response of our device, we use the slow-flow equations [cf. Eq. (3) and (B1)], and find the steady state amplitude response $R = \sqrt{u^2 + v^2}$ by setting $\dot{u} = \dot{v} = 0$, yielding [51]

$$\left[-\frac{\lambda^2}{4} + \left(\frac{\Gamma \omega}{\omega_0^2} \right)^2 + \left(1 - \frac{\omega^2}{\omega_0^2} + \frac{3}{4} \frac{\beta R^2}{\omega_0^2} \right)^2 \right] R^2 = 0. \quad (A1)$$

Equation (A1) has the trivial solution $R = 0$. For the case $R \neq 0$, we can divide Eq. (A1) by R^2 to obtain the nontrivial solutions

$$R(\omega) = \left(\frac{4\omega_0^2}{3\beta} \left[\left(\frac{\omega^2}{\omega_0^2} - 1 \right) \pm \left(\frac{\lambda^2}{4} - \frac{\Gamma^2 \omega^2}{\omega_0^4} \right)^{1/2} \right] \right)^{1/2}, \quad (A2)$$

when the radicands of both square roots are positive. Thus, the parametric amplitude response allows us (amongst other things) to extract the Duffing nonlinearity.

The outline of the Arnold tongue corresponds to the limit $R \to 0$ in Eq. (A2), leading to

$$\left(\omega^2 - \omega_0^2 \right)^2 - \frac{\lambda^2 \omega_0^4}{4} + \Gamma^2 \omega^2 = 0. \quad (A3)$$

Solving for the parametric drive yields

$$\lambda = 2\sqrt{ \frac{\Gamma^2 \omega^2}{\omega_0^4} + \left(1 - \frac{\omega^2}{\omega_0^2} \right)^2 }, \quad (A4)$$

where we kept the (physical) positive solution.

To extract our device parameters, we start by fitting Eq. (A4) to the outline of the Arnold tongue, see red dashed line in Fig. 5(c). For the fit, we replace $\lambda = U_\mathrm{p}/C$, where C is a constant converting the unitless parametric drive strength λ to the applied parametric voltage U_p. Doing so, we obtain the resonance frequency $\omega_0/2\pi = 1.1198294(3)\,\mathrm{MHz}$ and the energy decay rate $\Gamma/2\pi = 112(2)\,\mathrm{Hz}$ of our resonator, as well as the conversion constant $C = 9.88(5) \times 10^3\,\mathrm{V}$.

In a second step, we use the measured parametric response in Fig. 5(a) and fit it to Eq. (A2) in order to extract the Duffing nonlinearity $\beta = -9.894(4) \times 10^{16}\,(\mathrm{V\,s})^{-2}$, while fixing ω_0, Γ, and C to the previously fitted values.

2. Resonant sweep

We now extract the factor A, converting from an input voltage $\tilde{U}_\mathrm{r} = U_\mathrm{r} \cos(\omega_\mathrm{r} t)$ to an applied force F (in units $\mathrm{V\,s^{-2}}$), from the resonant response of our resonator.

To calibrate this, we consider the EOM for our resonator under near-resonant (but small, i.e., neglecting the Duffing term) drive [cf. Eq. (1)],

$$\ddot{x}(t) + \omega_0^2 x(t) + \Gamma \dot{x}(t) = A\tilde{U}_\mathrm{r}(t), \quad (A5)$$

where we replaced the forcing term by $F = A\tilde{U}_\mathrm{r}$. Taking the Fourier transform of Eq. (A5) yields

$$x(\omega) = A\tilde{U}_\mathrm{r}(\omega) \left[\omega_0^2 - \omega^2 - i\omega\Gamma \right]^{-1}, \quad (A6)$$

which provides a direct link between the voltage $\tilde{U}_\mathrm{r}$ applied to our device and the voltage $U_\mathrm{out} \equiv x$ we read out.

We can thus extract A by sweeping the frequency ω_r of a driving tone across the mechanical resonance of our resonator
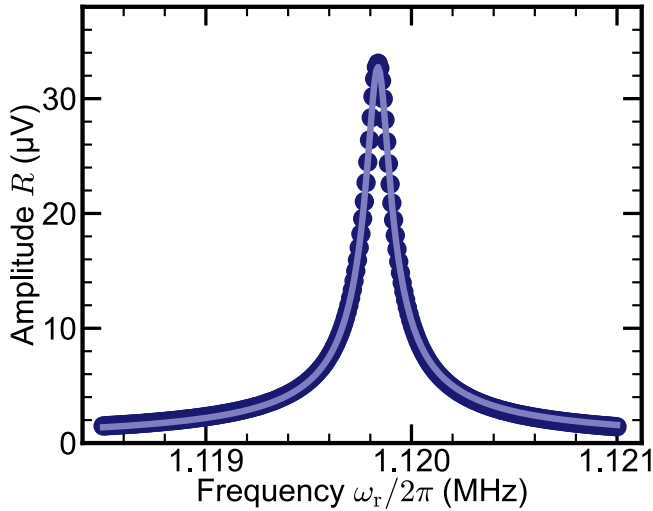
FIG. 6. Linear resonant response. An input voltage $\tilde{U}_r = U_r \cos(\omega_r t)$ with $U_r = 10\,\text{mV}$ is swept across the resonance frequency and the amplitude response $R = \sqrt{u^2 + v^2}$ at frequency ω_r is measured (dots). The data is fitted (line) according to Eq. (A6) with fixed $\Gamma/2\pi = 112\,\text{Hz}$, while ω_0 is left as a free parameter to account for small frequency drifts. We extract a value $A = 16.22(1) \times 10^6\,\text{s}^{-2}$.
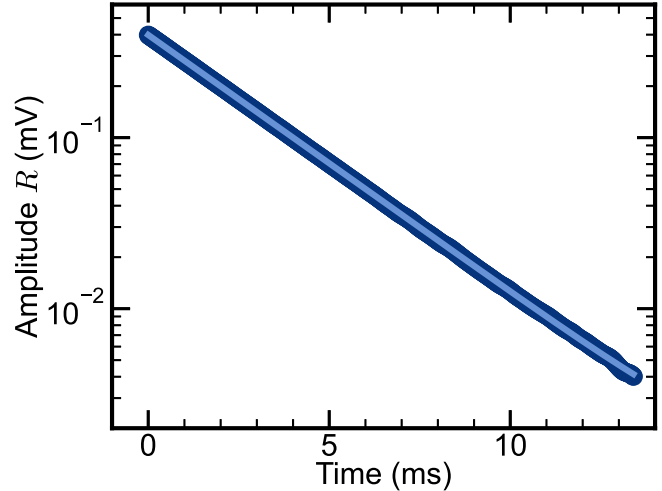

FIG. 7. Ringdown measurement. We drive our resonator with a near-resonant force to amplitude A_0 and then turn off the force, allowing us to measure our resonator's amplitude R decay as a function of time t (dark blue dots). We fit the linear damping model in Eq. (A7) to the data, yielding $\Gamma/2\pi \approx 110\,\text{Hz}$ and starting amplitude $A_0 \approx 0.40\,\text{mV}$. There are no deviations at large amplitudes, indicating that our oscillator's loss is dominated by linear damping.

and measuring its response. In Fig. 6, we fit the measured response with Eq. (A6) and obtain $A = 16.22(1) \times 10^6\,\text{s}^{-2}$.

3. Ringdown measurement

Here, we verify that our resonator experiences linear damping by taking a ringdown measurement. Solving the equation of motion of our resonator [Eq. (1)] with no drive ($\lambda = F = 0$), we obtain the amplitude R as a function of time t,

$$R(t) = A_0 e^{-\Gamma t/2}, \tag{A7}$$

with Γ the linear damping coefficient and $A_0 \equiv R(0)$ the initial amplitude. Note that the presence of a Duffing nonlinearity does not affect this amplitude decay [23,63].

We experimentally perform a ringdown measurement by displacing the oscillator to an initial amplitude A_0 with a near-resonant force, and then turning off this force. As shown in Fig. 7, the oscillator decays according to Eq. (A7). Nonlinear damping would appear as deviations from the exponential decay [23,54,63]. This justifies our assumption of purely linear damping for the reconstructions.

APPENDIX B: LINEARIZED MODEL

In this Appendix, we describe the method we use to obtain the EOMs for the rotating frame coordinates u and v, and the link between the symplectic norm and the ringdown trajectories. We first obtain the steady state solutions under parametric drive, then we linearize the EOMs in their vicinity. We solve the linearized EOMs to get analytical expressions for the resonators rotation frequency and direction around the attractors. The latter reveals a direct link between the ringdown rotation

and the symplectic norm of the corresponding final steady state. Finally, we show how to extract the symplectic norm from a ringdown measurement using the spectral response function.

1. Averaging method

As described in the main text, starting from Eq. (1), we move to a rotating frame with out-of-phase quadratures $u(t)$ and $v(t)$, defined via $x(t) = u(t)\cos(\omega_r t) - v(t)\sin(\omega_r t)$. Assuming that $u(t)$ and $v(t)$ vary slowly in time compared to the mechanical oscillations with frequency ω_r, we average the EOMs over the time $2\pi/\omega_r$ to obtain approximated EOMs for $u(t)$ and $v(t)$ [51],

$$\dot{u} = -\frac{\Gamma}{2}u - \delta v - \frac{3\beta}{8\omega_r}(u^2 v + v^3) - \frac{\lambda \omega_0^2}{4\omega_r}v,$$

$$\dot{v} = -\frac{\Gamma}{2}v + \delta u + \frac{3\beta}{8\omega_r}(u^3 + uv^2) - \frac{\lambda \omega_0^2}{4\omega_r}u, \tag{B1}$$

where we introduce the detuning $\delta \equiv (\omega_0^2 - \omega_r^2)/2\omega_r$. For simplicity, we also set $\psi = 0$ when moving from Eq. (1) to Eq. (B1). This phase ψ rotates the energy landscape in phase space around the origin with an angle of $\psi/2$, so the solutions for u or v calculated for $\psi = 0$ in this section can be rotated by an angle of $\psi/2$ to match the experimental results.

2. Linearization of the EOMs

To predict the motion of the resonator near an attractor, we linearize the slow-flow equations [Eq. (B1)] near the attractors [51,64]. To do so, we first determine the coordinates of the attractors (i.e., the stationary states of the system) in the

rotating frame by setting $\dot{u} = \dot{v} = 0$ in Eq. (B1). Solving the resulting coupled polynomial equations leads to five possible solutions [65,66]:

$$(u_{\text{f}}, v_{\text{f}})_1 = (0, 0),$$

$$(u_{\text{f}}, v_{\text{f}})_{2,3} = \left(\pm u_+, \pm \frac{u_+ \left(3\beta\lambda\omega_0^2 u_+^2 - 2\lambda^2\omega_0^4 + 4\Gamma^2\omega_{\text{r}}^2 + 4\lambda\omega_0^4 - 4\lambda\omega_0^2\omega_{\text{r}}^2\right)}{2\Gamma\omega_{\text{r}}\left(2\omega_{\text{r}}^2 - 2\omega_0^2 + \lambda\omega_0^2\right)} \right),$$

$$(u_{\text{f}}, v_{\text{f}})_{4,5} = \left(\pm u_-, \pm \frac{u_- \left(3\beta\lambda\omega_0^2 u_-^2 - 2\lambda^2\omega_0^4 + 4\Gamma^2\omega_{\text{r}}^2 + 4\lambda\omega_0^4 - 4\lambda\omega_0^2\omega_{\text{r}}^2\right)}{2\Gamma\omega_{\text{r}}\left(2\omega_{\text{r}}^2 - 2\omega_0^2 + \lambda\omega_0^2\right)} \right),$$

(B2)

where

$$u_\pm = \left[\frac{\beta\lambda\omega_0^2\left(2\lambda\omega_0^2\omega_{\text{r}}^2 + \lambda^2\omega_0^4 - 2\lambda\omega_0^4 - 4\Gamma^2\omega_{\text{r}}^2\right) \pm \sqrt{\beta^2\lambda^2\omega_0^4\left(2\omega_{\text{r}}^2 - 2\omega_0^2 + \lambda\omega_0^2\right)^2\left(\lambda^2\omega_0^4 - 4\Gamma^2\omega_{\text{r}}^2\right)}}{3\beta^2\lambda^2\omega_0^4} \right]^{1/2}.$$

(B3)

For any given set of parameters, a maximum of three of these solutions are stable, i.e., they act as attractors, cf. Fig. 3. To see if a solution is stable, we now introduce the displaced quadratures $(\tilde{u}, \tilde{v})_k \equiv (u - u_{\text{f}}, v - v_{\text{f}})_k$, relative to a given solution position $(u_{\text{f}}, v_{\text{f}})_k$, and linearize Eq. (B1) around one attractor by neglecting higher-order terms in $\tilde{u}$ and $\tilde{v}$. This procedure yields

$$\begin{pmatrix} \dot{\tilde{u}} \\ \dot{\tilde{v}} \end{pmatrix} = \underbrace{\begin{pmatrix} \frac{\partial\dot{u}}{\partial u} & \frac{\partial\dot{u}}{\partial v} \\ \frac{\partial\dot{v}}{\partial u} & \frac{\partial\dot{v}}{\partial v} \end{pmatrix}\Bigg|_{(u,v)=(u_{\text{f}}, v_{\text{f}})_k}}_{\mathbf{J}_{\text{f}}} \begin{pmatrix} \tilde{u} \\ \tilde{v} \end{pmatrix}.$$

(B4)

Here, $\mathbf{J}_{\text{f}}$ is the Jacobian of the slow-flow equations evaluated around the solution position $(u_{\text{f}}, v_{\text{f}})_k$, which takes the form

$$\mathbf{J}_{\text{f}} = \begin{pmatrix} -\frac{\Gamma}{2} - \frac{3\beta u_{\text{f}} v_{\text{f}}}{4\omega_{\text{r}}} & -\delta - \frac{3\beta(u_{\text{f}}^2 + 3v_{\text{f}}^2)}{8\omega_{\text{r}}} - \frac{\lambda\omega_0^2}{4\omega_{\text{r}}} \\ \delta + \frac{3\beta(3u_{\text{f}}^2 + v_{\text{f}}^2)}{8\omega_{\text{r}}} - \frac{\lambda\omega_0^2}{4\omega_{\text{r}}} & -\frac{\Gamma}{2} + \frac{3\beta u_{\text{f}} v_{\text{f}}}{4\omega_{\text{r}}} \end{pmatrix}.$$

(B5)

The Jacobian $\mathbf{J}_{\text{f}}$ describes the linearized forces acting in the rotating frame near a given solution. Solving the linear first-order differential equation given by Eq. (B4) leads to

$$\begin{pmatrix} \tilde{u} \\ \tilde{v} \end{pmatrix} = \zeta \mathbf{w}_+ e^{\mu_+ t} + \zeta^* \mathbf{w}_- e^{\mu_- t}.$$

(B6)

Here,

$$\zeta = \frac{1}{2}(v_{\text{i}} - v_{\text{f}}) - i\left(\frac{3\beta u_{\text{f}} v_{\text{f}}}{8\omega_{\text{r}}\omega_{\text{lin}}}(v_{\text{i}} - v_{\text{f}}) \right.$$
$$\left. + \frac{\left(9\beta u_{\text{f}}^2 + 3\beta v_{\text{f}}^2 + 4\omega_0^2 - 4\omega_{\text{r}}^2 - 2\lambda\omega_0^2\right)}{16\omega_{\text{r}}\omega_{\text{lin}}}(u_{\text{i}} - u_{\text{f}}) \right)$$

(B7)

is a constant which depends on the initial position $(u_{\text{i}}, v_{\text{i}})$ of the resonator in the rotating frame. Furthermore, we use in Eq. (B6) the Jacobian's eigenvectors

$$\mathbf{w}_\pm = \begin{pmatrix} \frac{-6\beta u_{\text{f}} v_{\text{f}} \pm 8i\omega_{\text{r}}\omega_{\text{lin}}}{9\beta u_{\text{f}}^2 + 3\beta v_{\text{f}}^2 + 4\omega_0^2 - 4\omega_{\text{r}}^2 - 2\lambda\omega_0^2} \\ 1 \end{pmatrix},$$

(B8)

and corresponding eigenvalues

$$\mu_\pm = -\Gamma/2 \pm i\omega_{\text{lin}},$$

(B9)

with the complex frequency

$$\omega_{\text{lin}} = \frac{1}{8\omega_{\text{r}}}\Big[27\beta^2 u_{\text{f}}^4 + 6\beta u_{\text{f}}^2\left(9\beta v_{\text{f}}^2 + 8\omega_0^2 - 8\omega_{\text{r}}^2 + 2\lambda\omega_0^2\right)$$
$$+ \left(3\beta v_{\text{f}}^2 + 4\omega_0^2 - 4\omega_{\text{r}}^2 - 2\lambda\omega_0^2\right)$$
$$\times \left(9\beta v_{\text{f}}^2 + 4\omega_0^2 - 4\omega_{\text{r}}^2 + 2\lambda\omega_0^2\right)\Big]^{1/2}.$$

(B10)

If the real part of one eigenvalue in Eq. (B9) is positive, Eq. (B6) diverges for $t \to \infty$ and $(u_{\text{f}}, v_{\text{f}})_k$ is an unstable state. If both real parts are negative, $(\tilde{u}, \tilde{v})$ converge to $(0, 0)$ and $(u_{\text{f}}, v_{\text{f}})_k$ is an attractor [51,64]. The theory results depicted in Figs. 2(b), 2(c)(i), and 2(c)(ii) are directly calculated using Eq. (B6).

The theory prediction for the frequency of the rotation around an attractor in Fig. 2(c)(iii) is analytically calculated using

$$\frac{1}{2\pi}\frac{d\tilde{\phi}}{dt} = \frac{\partial}{\partial t}\arctan\left(\frac{\tilde{v}}{\tilde{u}} \right)$$
$$= \frac{1}{2\pi}\frac{\tilde{u}(d\tilde{v}/dt) - \tilde{v}(d\tilde{u}/dt)}{\tilde{u}^2 + \tilde{v}^2}$$
$$= -\frac{|\zeta|^2\omega_{\text{lin}}}{\pi}\frac{ds^2}{\tilde{u}^2 + \tilde{v}^2}e^{-\Gamma t},$$

(B11)

with the symplectic norm defined as

$$ds^2 \equiv i(w_{+,1}w_{-,2} - w_{-,1}w_{+,2}),$$

(B12)

and where $w_{\pm,l}$ is the lth entry of $\mathbf{w}_\pm$. The sign of ds^2 therefore decides the rotational sense of the ringdown. Note that Eq. (B11) only needs $\tilde{u}$ and $\tilde{v}$ to be of the form described in Eq. (B6). The explicit form of ω_{lin} or ζ is not relevant. The connection between ringdown chirality and symplectic norm therefore holds for more general systems than the studied parametric oscillator.

We now show that this quantity is identical to the symplectic norm derived for quantum driven-dissipative systems, which allows to classify stable states in driven-dissipative systems [29,30,67].

3. Symplectic norm

To see that the symplectic norm [cf. Eq. (B12)] is the same as the one defined in quantum driven-dissipative systems, we transform our definition of the symplectic norm to the form commonly used in quantum optics [29,30,67]. First, we express the rotating frame coordinates $\tilde{u}(t)$ and $\tilde{v}(t)$ in terms of the complex coordinate $\alpha(t)$ and its complex conjugate $\alpha^*(t)$ via the transformation matrix $\mathbf{S}$:

$$
\begin{pmatrix} \tilde{u} \\ \tilde{v} \end{pmatrix} = \underbrace{\sqrt{\frac{\hbar}{2m\omega_0}} \begin{pmatrix} 1 & 1 \\ i & -i \end{pmatrix}}_{\equiv \mathbf{S}^{-1}} \begin{pmatrix} \alpha \\ \alpha^* \end{pmatrix}. \tag{B13}
$$

This basis change can be interpreted as moving to the mean-field limit of bosonic creation and annihilation operators of a quantum harmonic oscillator representing the quadratures $\tilde{u}(t)$ and $\tilde{v}(t)$ (i.e., $\alpha = \langle a \rangle$ with a bosonic annihilation operator a and expectation value $\langle \ldots \rangle$).

Note that the $\sqrt{\hbar/2m\omega_0}$ prefactor is the same for both quadratures due to our definition of $\tilde{u}$ and $\tilde{v}$ sharing the same units. This prefactor leads to

$$
\mathbf{S}^{-1} = \frac{\hbar}{m\omega_0} \mathbf{S}^\dagger, \tag{B14}
$$

implying that $\mathbf{S}$ is not unitary and therefore not a norm-preserving transformation. This will later be accounted for by scaling the vectors in the new basis, and has no consequences for the sign of the symplectic norm, which is the relevant quantity for us.

We use the transformation introduced in Eqs. (B4) and (B13) to find the equations of motion for α and α^*:

$$
i\mathbf{S}\begin{pmatrix} \dot{\tilde{u}} \\ \dot{\tilde{v}} \end{pmatrix} = i\mathbf{S}\mathbf{J}_{\mathrm{f}}\begin{pmatrix} \tilde{u} \\ \tilde{v} \end{pmatrix} \Rightarrow i\begin{pmatrix} \dot{\alpha} \\ \dot{\alpha}^* \end{pmatrix} = \underbrace{i\mathbf{S}\mathbf{J}_{\mathrm{f}}\mathbf{S}^{-1}}_{\equiv \mathbf{D}}\begin{pmatrix} \alpha \\ \alpha^* \end{pmatrix}. \tag{B15}
$$

We multiplied both sides of Eq. (B13) with a complex factor i in order to bring Eq. (B15) into a form where the so-called dynamic matrix $\mathbf{D}$ [68] of the system can be directly read out. This is crucial as the symplectic norm defined in Ref. [30] is formulated in terms of the eigenvectors of the dynamic matrix.

The eigenvectors $\mathbf{v}_\pm$ of the dynamic matrix $\mathbf{D}$ can be calculated using the eigenvectors $\mathbf{w}_\pm$ of the Jacobian $\mathbf{J}_{\mathrm{f}}$:

$$
\mathbf{J}_{\mathrm{f}}\mathbf{w}_\pm = \mu_\pm \mathbf{w}_\pm
$$
$$
\Rightarrow i\,\mathbf{S}\mathbf{J}_{\mathrm{f}}\mathbf{S}^{-1}\mathbf{S}\mathbf{w}_\pm = i\,\mu_\pm \mathbf{S}\mathbf{w}_\pm
$$
$$
\Rightarrow i\,\mathbf{D}\mathbf{S}\mathbf{w}_\pm = i\,\mu_\pm \mathbf{S}\mathbf{w}_\pm
$$
$$
\Rightarrow \mathbf{D}\left(\sqrt{\frac{m\omega_0}{\hbar}}\mathbf{v}_\pm\right) = i\mu_\pm\left(\sqrt{\frac{m\omega_0}{\hbar}}\mathbf{v}_\pm\right). \tag{B16}
$$

In the last line, we used the definition of $\mathbf{D}$ from Eq. (B15) and introduced an additional factor of $\sqrt{m\omega_0/\hbar}$ to ensure that $|\mathbf{w}_\pm| = |\mathbf{v}_\pm|$, accounting for the fact that $\mathbf{S}$ is not a unitary transformation, cf. Eq. (B14).

Since $\mathbf{w}_+ = \mathbf{w}_-^*$, this implies that $\mathbf{v}_+ = \mathbf{v}_-^*$, and we have $\mathbf{w}_+^\dagger = \mathbf{w}_-^T$, as well as $\mathbf{v}_+^\dagger = \mathbf{v}_-^T$ (with T denoting transpose), allowing us to rewrite the classical symplectic norm defined
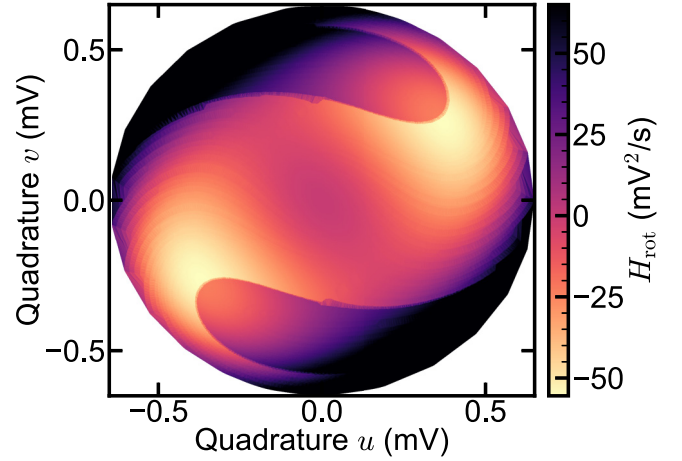

FIG. 8. Hamiltonian reconstruction before adjusting the offset C_k of each attractor. After using Eq. (5) to recover the relative Hamiltonian landscape along each ringdown trajectory and setting the end point of each ringdown to $C_k = 0$, we obtain a discontinuous Hamiltonian. The clear discontinuity happens at the separatrix of the system since the offset between the different attractors $C_k - C_{k+1}$ has yet to be found.

in Eq. (B12) as

$$
ds^2 = (w_{-,1}, w_{-,2})\begin{pmatrix} 0 & -i \\ i & 0 \end{pmatrix}\begin{pmatrix} w_{+,1} \\ w_{+,2} \end{pmatrix}
$$
$$
= (w_{-,1}, w_{-,2})\mathbf{S}^\dagger(\mathbf{S}^\dagger)^{-1}\begin{pmatrix} 0 & -i \\ i & 0 \end{pmatrix}\mathbf{S}^{-1}\mathbf{S}\begin{pmatrix} w_{+,1} \\ w_{+,2} \end{pmatrix}
$$
$$
= (\mathbf{S}\mathbf{w}_+)^\dagger(\mathbf{S}^\dagger)^{-1}\begin{pmatrix} 0 & -i \\ i & 0 \end{pmatrix}\mathbf{S}^{-1}\mathbf{S}\mathbf{w}_+
$$
$$
= \mathbf{v}_+^\dagger \mathbf{I}_- \mathbf{v}_+, \tag{B17}
$$

with $\mathbf{I}_- = \mathrm{diag}(1, -1)$, and where we used $\mathbf{v}_+ = \mathbf{S}\mathbf{w}_+$. Since the symplectic norm is real valued, one could also calculate it using $\mathbf{v}_-$, yielding the same result:

$$
ds^2 = (ds^2)^\dagger = (\mathbf{v}_+^\dagger \mathbf{I}_- \mathbf{v}_+)^\dagger = \mathbf{v}_-^\dagger \mathbf{I}_- \mathbf{v}_-. \tag{B18}
$$

Equations (B17) and (B18) show that the (classical) symplectic norm defined in Eq. (B12) coincides exactly with the symplectic norm introduced in Ref. [30]. As the sign of Eq. (B11) is determined by ds^2, the rotational sense of a ringdown is directly linked with the sign of the symplectic norm of the attractor. Since the sign of the symplectic norm of an attractor is positive (negative) for a minimum (maximum) of the underlying energy landscape [29,30], the rotational sense of the ringdown can be used to differ between maxima and minima in the rotating frame energy.

4. Spectral response

Having established a link between the rotational sense of ringdowns and the symplectic norm, we derive the spectral response of fluctuations around an attractor. This spectral response also allows us to extract the symplectic norm from ringdown measurements.
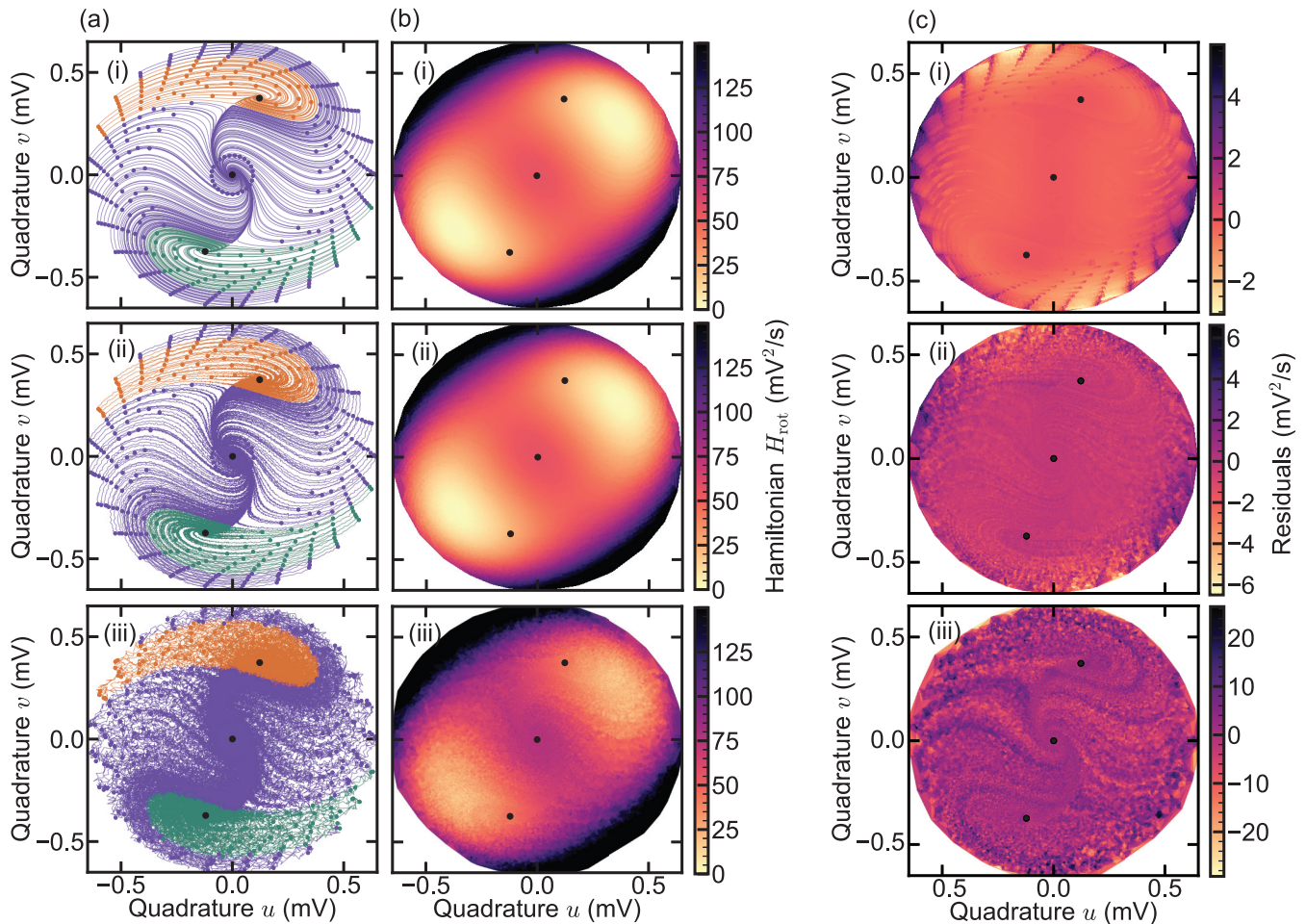
FIG. 9. Reconstructed Hamiltonians and residuals with added noise. (a) Multiple ringdowns in phase space for the mixed parametric phase, with (i) no added noise (i.e., same as measured in Fig. 3), and added Gaussian noise in post processing at each measured points with standard deviation (ii) $\sigma_V \approx 2 \times 10^{-3}$ mV and (iii) $\sigma_V \approx 1 \times 10^{-2}$ mV. (b) The corresponding reconstructed Hamiltonian $H_{\rm rot}$. (c) The residual $H_{\rm rot} - H_{\rm rot}^{\rm fit}$, with the corresponding fitted Hamiltonian $H_{\rm rot}^{\rm fit}$ of each reconstruction. For a better estimate of our reconstruction performance, we use the overall offset, Duffing nonlinearity β, natural frequency ω_0, parametric driving strength λ, and parametric drive angle ψ as fit parameters.

In analogy to driven-dissipative quantum systems [29,30], we first introduce the correlator function

$$G^c(t' - t) = \Theta(t' - t)\langle \tilde{v}(t)\tilde{u}(t') - \tilde{u}(t)\tilde{v}(t')\rangle_t$$

$$= \Theta(t' - t)\frac{2ds^2|\zeta|^2}{\Gamma} e^{-\frac{\Gamma}{2}(t'-t)} \sin(\omega_{\rm lin}(t' - t)),$$
(B19)

where $\Theta(t - t')$ is the Heavyside step-function. The function G^c correlates the displaced quadratures $\tilde{u}(t)$ and $\tilde{v}(t')$ at different times to capture the rotational sense of a ringdown near an attractor. This correlator is reminiscent of Eq. (B12), and is analogous to a retarded Green's function in driven-dissipative quantum systems, correlating at different times the creation and annihilation of bosons on top of a stable solution. Note that the second equality in Eq. (B19) holds in the limit of the linearization procedure presented earlier. The sign of the symplectic norm can now be read out directly by inspecting the peaks and dips of the spectral function [29,30,34]. This spectral response is related to the imaginary part of the Fourier

transform of the Green's function $G^c(\omega)$ via

$$\mathcal{A}(\omega) = -2\text{Im}[G^c(\omega)].$$
(B20)

Explicitly computing Eq. (B20) using Eq. (B19) yields the spectral response of our system:

$$\mathcal{A}(\omega) = \frac{|\zeta|^2 ds^2}{2}\left[\frac{1}{(\omega - \omega_{\rm lin})^2 + \frac{\Gamma^2}{4}} - \frac{1}{(\omega + \omega_{\rm lin})^2 + \frac{\Gamma^2}{4}}\right].$$
(B21)

A peak (dip) of $\mathcal{A}$ at positive frequencies therefore corresponds to a positive (negative) symplectic norm and hence to a minimum (maximum) of the rotating frame energy landscape $H_{\rm rot}$ at $(u_{\rm f}, v_{\rm f})$.

APPENDIX C: DETAILS OF THE HAMILTONIAN RECONSTRUCTION

In this section, we provide further details on the Hamiltonian reconstruction process. We start the reconstruction by using a single ringdown measurement with the quadratures $u_j(t_j)$ and $v_j(t_j)$ measured at discrete times t_j. Assuming

that our device is linearly damped, and using the extracted damping Γ, we calculate the change in the Hamiltonian $\Delta H_{\text{rot}}(u_j, v_j)$ at each coordinates along the ringdown path by numerically integrating Eq. (5).

We then find the attractor k, e.g., $k = 1, 2, 3$ for the case of three attractors, in which the resonator rings down into by looking at the final value $(u_{\text{f}}, v_{\text{f}})_k$. We fix the Hamiltonian $H_{\text{rot}}(u_{\text{f}}, v_{\text{f}}) = C_k$ at the final coordinate $(u_{\text{f}}, v_{\text{f}})_k$ to an arbitrary value C_k. To do so, we add a constant offset to the Hamiltonian change ΔH_{rot} calculated for the ringdown. This will ensure that the Hamiltonian is singled-valued at each attractor, i.e., $H_{\text{rot}}(u_{\text{f}}, v_{\text{f}})$ is the same for each ringdown ending up in the same attractor. At this stage, we simply set $C_k = 0$.

As a second step, we repeat the integration procedure for all ringdown measurements and check if the final value of each ringdown $(u_{\text{f}}, v_{\text{f}})_k$ is the same as the first ringdown, or if it ends up at another attractor. If it is another attractor, we label the new attractor as $k + 1$, and add an arbitrary value C_{k+1} to the trace, which we will later adjust. We repeat this procedure for all measured ringdowns, allowing to find the Hamiltonian change for all the ringdown paths, as shown in Fig. 8 for an example with three attractors.

We generally find discontinuities in the Hamiltonian reconstruction at the separatrices between different attractors, see Fig. 8. Such discontinuities are unphysical and stem from our choice to set all offsets to $C_k = 0$. As a last step of the reconstruction, we thus need to find the relative height $C_k - C_{k+1}$ between the attractors such that the discontinuities disappear. In practice, we fix one of the constants (e.g., $C_1 = 0$), and vary the constant offsets C_k of the other attractors (C_2 and C_3 in Fig. 8) until the Hamiltonian is smooth (i.e., such that the second differentials of H_{rot} with respect to u and v are minimized). We furthermore set the minimum of $H_{\text{rot}} = 0$, yielding Fig. 3(a)(iii). For our demonstration examples, this optimization was done manually.

APPENDIX D: RECONSTRUCTION ERROR

In this section, we discuss different possible sources of noise, e.g. frequency noise, thermomechanical noise, and detection noise, and how they can corrupt our Hamiltonian reconstruction protocol. In particular, we quantify the effect of measurement noise.

First, frequency drifts occur when the resonance frequency of a system is not stable over time, owing to e.g. temperature changes. Such drifts lead to a change in the actual Hamiltonian of the resonator. For this reason, any Hamiltonian reconstruction can only be meaningful when frequency drift is small enough to be ignored over the full measurement time scale. Our mechanical resonator experiences small frequency drifts (typically <1 Hz $\ll \Gamma/2\pi$) over the duration (~ 1 h) of a reconstruction measurement, and should only have a small impact on our results.

A second important noise source is the thermomechanical force noise. In our device, the standard deviation of the measured voltage due to thermomechanical force noise is too small to be measured relative to the detection noise. Large force noise would lead to changes in the amplitude and phase of the oscillation over timescales of the ringdown time $\tau = 2\Gamma^{-1}$. This timescale τ is also the typical time for
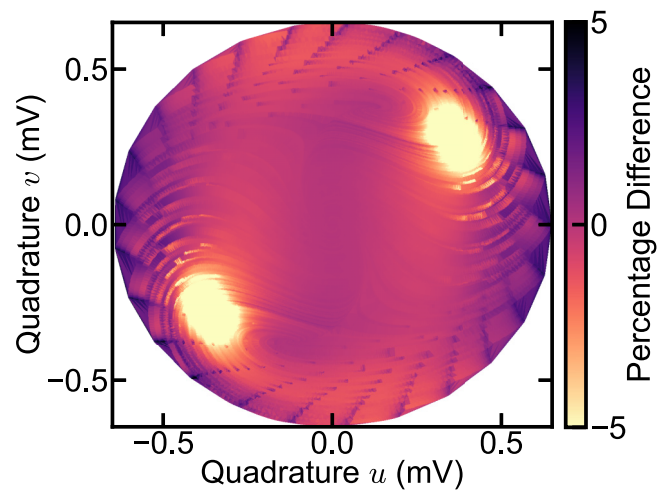

FIG. 10. Percentage residuals. Percentage residuals $(H_{\text{rot}} - H_{\text{rot}}^{\text{theo}})/H_{\text{rot}}^{\text{theo}}$ of the reconstructed Hamiltonian landscape when driven far detuned and above threshold, with no added noise. The theoretical reconstructed landscape is obtained using ψ, ω_0, β and C as fit parameters, showing a few percents of deviation away from the minima. The scale of the color bar is limited to $\pm 5\%$ for visibility.

a ringdown trajectory. Thermomechanical force noise would therefore only have a minor impact on the positions of consecutive points along a ringdown, and its main role will be to change the initial condition of the trajectory. As long as the initial conditions are measured correctly, such changes would not affect the reconstruction significantly. In systems with dominant thermomechanical noise, probabilistic methods are more suitable than our ringdown procedure [6–13].
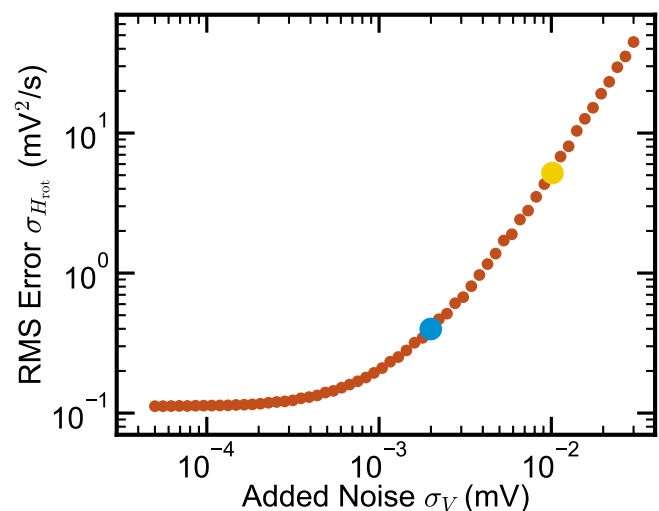

FIG. 11. Reconstruction error. The root-mean-square error [Eq. (D1)] of the reconstructed Hamiltonian as a function of the standard deviation of the added noise. The larger blue and yellow dots indicate the added noise for the reconstruction in Figs. 9(ii) and 9(iii), respectively. For reference, the standard deviation of our measurement is $\sigma_V \approx 9 \times 10^{-5}$ mV, indicating that an order of magnitude of noise can be added without significantly affecting the reconstructed error.
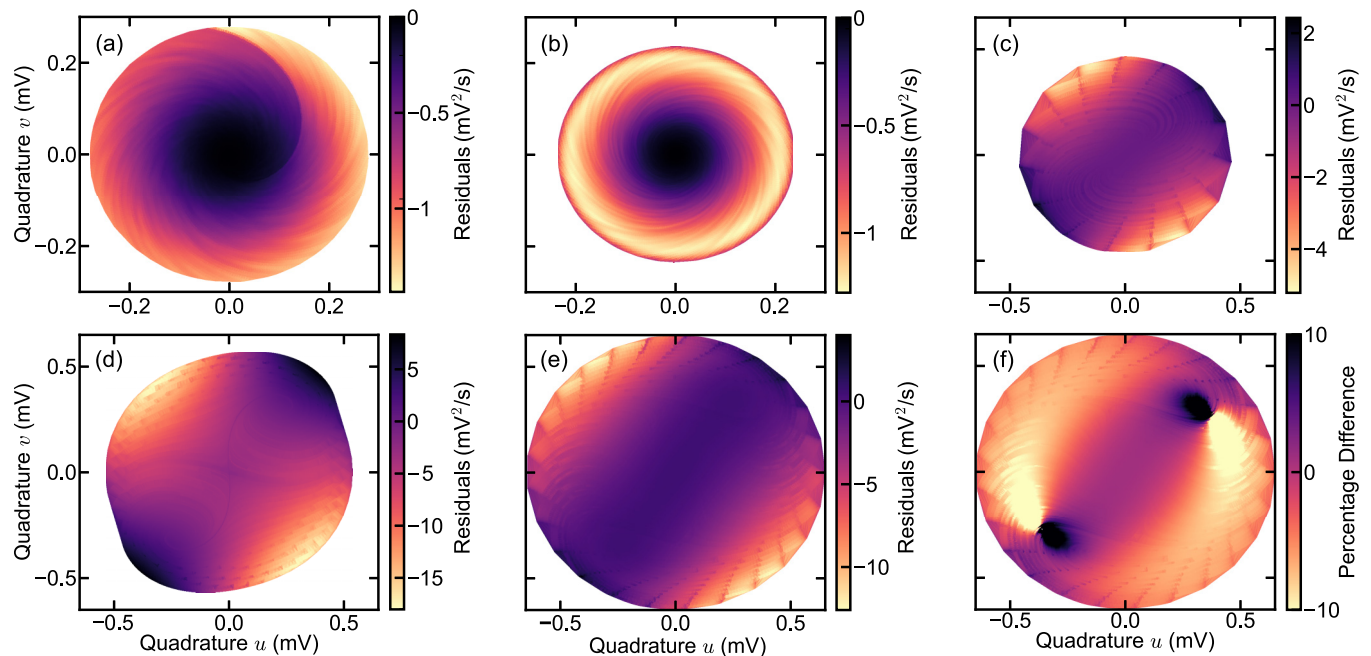
FIG. 12. Residuals $H_{\text{rot}} - H_{\text{rot}}^{\text{theo}}$ of the Hamiltonian reconstructions presented in the main text. (a) Residuals for the undriven oscillator at positive detuning for the reconstruction H_{rot} shown in Fig. 1(d). (b) Residual for the undriven oscillator at negative detuning for the reconstruction of Fig. 1(e). (c) Residuals for the the parametric oscillator driven below threshold, corresponding to Fig. 3(i). (d) Residuals for the parametric oscillator driven above threshold, corresponding to Fig. 3(ii). (e) Residuals for the parametric oscillator driven above threshold and far detuned, corresponding to Fig. 3(iii). (f) Residuals $(H_{\text{rot}} - H_{\text{rot}}^{\text{theo}})/H_{\text{rot}}^{\text{theo}}$ for the same measurement as (e) but now expressed as percentage. The scale of the color bar is limited to ±10% for visibility.

A third important source of noise is detection noise, which is typically approximately white over the spectral range of interest. White noise affects each data point of a trajectory in a random and uncorrelated manner and can seriously affect the reconstruction. To assess the impact of white readout noise, we add Gaussian-distributed white noise with a given standard deviation σ_V to our measured data in post processing. The best estimated Hamiltonian $H_{\text{rot}}^{\text{fit}}$ is obtained by fitting the theoretical model [Eq. (4)] to the reconstructed Hamiltonian. We use an overall offset, Duffing non-linearity β, natural frequency ω_0, parametric driving strength λ, and parametric drive angle ψ as fit parameters.

The fidelity of our reconstruction is quantified via the standard deviation of the reconstructed Hamiltonian H_{rot} relative to the fitted Hamiltonian $H_{\text{rot}}^{\text{fit}}$ over the full measured phase-space (u_j, v_j):

$$\sigma_{H_{\text{rot}}} = \sqrt{\frac{\sum_{j=1}^{N} \left[H_{\text{rot}}(u_j, v_j) - H_{\text{rot}}^{\text{fit}}(u_j, v_j)\right]^2}{N}}, \qquad \text{(D1)}$$

with $N \approx 10^6$ the number of sampled points.

In Fig. 9(a)(i), we show a set of ringdown trajectories with an intrinsic measurement noise standard deviation of roughly $\sigma_V^{\text{int}} \approx 9 \times 10^{-5}$ mV. We add white noise with standard deviation σ_V to this data set in post processing, and show the results for $\sigma_V \approx 2 \times 10^{-3}$ mV in Fig. 9(a)(ii), and for $\sigma_V \approx 1 \times 10^{-2}$ mV in Fig. 9(a)(iii). The corresponding reconstructed Hamiltonians H_{rot} are shown in Fig. 9(b). The reconstruction still looks qualitatively good in (ii), regardless of the fact that we have one order of magnitude higher noise than in (i). In (iii), the higher noise clearly affects the

reconstruction. However, the qualitative features, such as number and position of stable solutions, are still reconstructed correctly.

We compare the residuals $H_{\text{rot}} - H_{\text{rot}}^{\text{fit}}$ of the fit in Fig. 9(c), showing little systematic structure in the residuals even at $\sigma_V \approx 2 \times 10^{-3}$ mV. The larger deviations near the edge on the reconstructions are due to the lower density of measurement points in these areas. The percentage residuals of Fig. 9(i) are presented in Fig. 10, showing only a few percents of deviation in the reconstructed Hamiltonian away from the minima (where the energy is close to zero, leading to large percentage errors).

The reconstructed Hamiltonian can also be used to extract the system parameters. When no noise is added and the theoretical Hamiltonian is fitted to the reconstructed Hamiltonian, cf. Fig. 9(i), we obtain a natural frequency $\omega_0/2\pi = 1.11983354(2)$ MHz, a Duffing nonlinearity $\beta = -9.8788(2) \times 10^{16}$ (V · s)$^{-2}$, and a parametric drive conversion factor $C = 10.6248(2) \times 10^3$ V. The errors quoted on these parameters are the statistical errors from the fit, which underestimate the total error. They do not take into account parameters drifting during the measurement, or the error on the damping Γ which is assumed during the reconstruction. This could explain why the fitted parameters are several standard deviations away from the independent calibration of Appendix A.

The reconstruction can be further quantified using the root-mean-square (RMS) error, given by Eq. (D1). We calculate this quantity in Fig. 11 for varying added noise. Importantly, there is no significant increase in the RMS error for an order of magnitude greater noise than we observe in our experiment.

In summary, the qualitative reconstruction of the Hamiltonian is very robust against measurement noise.

APPENDIX E: HAMILTONIAN RECONSTRUCTION RESIDUALS

Here, we present the residuals of the energy landscapes H_{rot} reconstructed in the main text.

First, in Figs. 12(a) and 12(b), we show the residuals $H_{\text{rot}} - H_{\text{rot}}^{\text{theo}}$ corresponding to the Hamiltonian reconstructions of Figs. 1(d) and 1(e), respectively. The theoretical prediction $H_{\text{rot}}^{\text{theo}}$ is given by Eq. (4), using parameters obtained from independent calibration measurements—see Appendix A. Note that there are structures in the residuals, which can be attributed to drifts (e.g., in the natural frequency ω_0) over the course of the measurements, or small errors in the calibrated parameters. Larger residuals appear further away from the stationary state ($u_{\text{f}} = 0$, $v_{\text{f}} = 0$), which is expected since the Hamiltonian is referenced to this point, so the error accumulates for data points away from this stationary state.

The residuals corresponding to the reconstructed Hamiltonians of Figs. 3(i), 3(ii), and 3(iii) are shown in Figs. 12(c), 12(d) and 12(e), respectively. We stress that the theoretical predictions use only the parametric drive phase ψ as a fit parameter, while the other parameters are obtained from independent calibrations. We also show in Fig. 12(f) the same residuals as Fig. 12(e), but now in terms of percentage. Using precalibrated parameters, the deviations are smaller than $\sim 10\%$ away from the minima. Note that this error is reduced to a few percent if the parameters are fitted instead, as shown in Appendix D, cf. Fig. 10.

Importantly, our method provides good qualitative agreement with the predicted Hamiltonian landscapes of various cases, allowing us to discern all the general features (e.g., minima and maxima) of the energy landscape.

[1] M. T. Cuairan, J. Gieseler, N. Meyer, and R. Quidant, Precision calibration of the duffing oscillator with phase control, Phys. Rev. Lett. **128**, 213601 (2022).

[2] E. Bairey, I. Arad, and N. H. Lindner, Learning a local Hamiltonian from local measurements, Phys. Rev. Lett. **122**, 020504 (2019).

[3] X.-L. Qi and D. Ranard, Determining a local Hamiltonian from a single eigenstate, Quantum **3**, 159 (2019).

[4] Z. Lin, K. Inomata, K. Koshino, W. D. Oliver, Y. Nakamura, J. S. Tsai, and T. Yamamoto, Josephson parametric phase-locked oscillator and its application to dispersive readout of superconducting qubits, Nat. Commun. **5**, 4480 (2014).

[5] K. Siva, G. Koolstra, J. Steinmetz, W. P. Livingston, D. Das, L. Chen, J. M. Kreikebaum, N. J. Stevenson, C. Jünger, D. I. Santiago, I. Siddiqi, and A. N. Jordan, Time-dependent Hamiltonian reconstruction using continuous weak measurements, PRX Quantum **4**, 040324 (2023).

[6] E. Florin, A. Pralle, E. Stelzer, and J. Hörber, Photonic force microscope calibration by thermal noise analysis, Appl. Phys. A **66**, S75 (1998).

[7] L. I. McCann, M. Dykman, and B. Golding, Thermally activated transitions in a bistable three-dimensional optical trap, Nature (London) **402**, 785 (1999).

[8] H. B. Chan and C. Stambaugh, Activation barrier scaling and crossover for noise-induced switching in micromechanical parametric oscillators, Phys. Rev. Lett. **99**, 060601 (2007).

[9] S. Jeney, E. H. Stelzer, H. Grubmüller, and E.-L. Florin, Mechanical properties of single motor molecules studied by three-dimensional thermal force probing in optical tweezers, ChemPhysChem **5**, 1150 (2004).

[10] Y. Tanaka, S. Kaneda, and K. Sasaki, Nanostructured potential of optical trapping using a plasmonic nanoblock pair, Nano Lett. **13**, 2146 (2013).

[11] L. Rondin, J. Gieseler, F. Ricci, R. Quidant, C. Dellago, and L. Novotny, Direct measurement of kramers turnover with a levitated nanoparticle, Nat. Nanotechnol. **12**, 1130 (2017).

[12] N. Zijlstra, D. Nettels, R. Satija, D. E. Makarov, and B. Schuler, Transition path dynamics of a dielectric particle in a bistable optical trap, Phys. Rev. Lett. **125**, 146001 (2020).

[13] A. Militaru, M. Innerbichler, M. Frimmer, F. Tebbenjohanns, L. Novotny, and C. Dellago, Escape dynamics of active particles in multistable potentials, Nat. Commun. **12**, 2446 (2021).

[14] P. Wu, R. Huang, C. Tischer, A. Jonas, and E.-L. Florin, Direct measurement of the nonconservative force field generated by optical tweezers, Phys. Rev. Lett. **103**, 108101 (2009).

[15] L. Pérez García, J. Donlucas Pérez, G. Volpe, A. V. Arzola, and G. Volpe, High-performance reconstruction of microscopic force fields from Brownian trajectories, Nat. Commun. **9**, 5166 (2018).

[16] T. L. Heugel, R. Chitra, A. Eichler, and O. Zilberberg, Proliferation of unstable states and their impact on stochastic out-of-equilibrium dynamics in two coupled Kerr parametric oscillators, Phys. Rev. E **109**, 064308 (2024).

[17] P. Álvarez, D. Pittilini, F. Miserocchi, S. Raamamurthy, G. Margiani, O. Ameye, J. del Pino, O. Zilberberg, and A. Eichler, A biased ising model using two coupled Kerr parametric oscillators with external force, Phys. Rev. Lett. **132**, 207401 (2024).

[18] B. Swingle, Unscrambling the physics of out-of-time-order correlators, Nat. Phys. **14**, 988 (2018).

[19] P. D. Blocher, S. Asaad, V. Mourik, M. A. I. Johnson, A. Morello, and K. Mølmer, Measuring out-of-time-ordered correlation functions without reversing time evolution, Phys. Rev. A **106**, 042429 (2022).

[20] A. Bachtold, J. Moser, and M. I. Dykman, Mesoscopic physics of nanomechanical systems, Rev. Mod. Phys. **94**, 045005 (2022).

[21] T. Antoni, K. Makles, R. Braive, T. Briant, P.-F. Cohadon, I. Sagnes, I. Robert-Philip, and A. Heidmann, Nonlinear mechanics with suspended nanomembranes, Europhys. Lett. **100**, 68005 (2012).

[22] P. M. Polunin, Y. Yang, M. I. Dykman, T. W. Kenny, and S. W. Shaw, Characterization of mems resonator nonlinearities

using the ringdown response, J. Microelectromech. Syst. **25**, 297 (2016).

[23] L. Catalini, M. Rossi, E. C. Langman, and A. Schliesser, Modeling and observation of nonlinear damping in dissipation-diluted nanomechanical resonators, Phys. Rev. Lett. **126**, 174101 (2021).

[24] A. Morales, P. Zupancic, J. Léonard, T. Esslinger, and T. Donner, Coupling two order parameters in a quantum gas, Nat. Mater. **17**, 686 (2018).

[25] I. Kozinsky, H. W. C. Postma, O. Kogan, A. Husain, and M. L. Roukes, Basins of attraction of a nonlinear nanomechanical resonator, Phys. Rev. Lett. **99**, 207201 (2007).

[26] Y. Yan, X. Dong, L. Huang, K. Moskovtsev, and H. B. Chan, Energy transfer into period-tripled states in coupled electromechanical modes at internal resonance, Phys. Rev. X **12**, 031003 (2022).

[27] J. Woo and R. Landauer, Fluctuations in a parametrically excited subharmonic oscillator, IEEE J. Quantum Electron. **7**, 435 (1971).

[28] M. I. Dykman, C. M. Maloney, V. N. Smelyanskiy, and M. Silverstein, Fluctuational phase-flip transitions in parametrically driven oscillators, Phys. Rev. E **57**, 5202 (1998).

[29] M. Soriente, R. Chitra, and O. Zilberberg, Distinguishing phases using the dynamical response of driven-dissipative light-matter systems, Phys. Rev. A **101**, 023823 (2020).

[30] M. Soriente, T. L. Heugel, K. Omiya, R. Chitra, and O. Zilberberg, Distinctive class of dissipation-induced phase transitions and their universal characteristics, Phys. Rev. Res. **3**, 023100 (2021).

[31] F. Ferri, R. Rosa-Medina, F. Finger, N. Dogra, M. Soriente, O. Zilberberg, T. Donner, and T. Esslinger, Emerging dissipative phases in a superradiant quantum gas with tunable decay, Phys. Rev. X **11**, 041046 (2021).

[32] A. Roy, S. Jahani, C. Langrock, M. Fejer, and A. Marandi, Spectral phase transitions in optical parametric oscillators, Nat. Commun. **12**, 835 (2021).

[33] G.-Q. Zhang, Z. Chen, W. Xiong, C.-H. Lam, and J. Q. You, Parity-symmetry-breaking quantum phase transition via parametric drive in a cavity magnonic system, Phys. Rev. B **104**, 064423 (2021).

[34] O. Scarlatella, A. A. Clerk, and M. Schiro, Spectral functions and negative density of states of a driven-dissipative nonlinear quantum resonator, New J. Phys. **21**, 043040 (2019).

[35] H. Li, Y. Tong, H. Ni, T. Gefen, and L. Ying, Heisenberg-limited Hamiltonian learning for interacting bosons, arXiv:2307.04690.

[36] N. Wiebe, C. Granade, C. Ferrie, and D. Cory, Quantum Hamiltonian learning using imperfect quantum resources, Phys. Rev. A **89**, 042314 (2014).

[37] H.-Y. Huang, Y. Tong, D. Fang, and Y. Su, Learning many-body Hamiltonians with Heisenberg-limited scaling, Phys. Rev. Lett. **130**, 200403 (2023).

[38] M. Agarwal, S. A. Chandorkar, H. Mehta, R. N. Candler, B. Kim, M. A. Hopcroft, R. Melamud, C. M. Jha, G. Bahl, G. Yama, T. W. Kenny, and B. Murmann, A study of electrostatic force nonlinearities in resonant microstructures, Appl. Phys. Lett. **92**, 104106 (2008).

[39] S. Schmid, L. G. Villanueva, and M. L. Roukes, *Fundamentals of Nanomechanical Resonators* (Springer, Berlin, 2016), Vol. 49.

[40] J. M. L. Miller, D. D. Shin, H.-K. Kwon, S. W. Shaw, and T. W. Kenny, Phase control of self-excited parametric resonators, Phys. Rev. Appl. **12**, 044053 (2019).

[41] Ž. Nosan, P. Märki, N. Hauff, C. Knaut, and A. Eichler, Gate-controlled phase switching in a parametron, Phys. Rev. E **99**, 062205 (2019).

[42] M. Marthaler and M. I. Dykman, Switching via quantum activation: A parametrically modulated oscillator, Phys. Rev. A **73**, 042108 (2006).

[43] D. Ryvkine and M. I. Dykman, Resonant symmetry lifting in a parametrically modulated oscillator, Phys. Rev. E **74**, 061118 (2006).

[44] I. Mahboob and H. Yamaguchi, Bit storage and bit flip operations in an electromechanical oscillator, Nat. Nanotechnol. **3**, 275 (2008).

[45] C. M. Wilson, T. Duty, M. Sandberg, F. Persson, V. Shumeiko, and P. Delsing, Photon generation in an electromagnetic cavity with a time-dependent boundary, Phys. Rev. Lett. **105**, 233907 (2010).

[46] A. Leuch, L. Papariello, O. Zilberberg, C. L. Degen, R. Chitra, and A. Eichler, Parametric symmetry breaking in a nonlinear resonator, Phys. Rev. Lett. **117**, 214101 (2016).

[47] J. Gieseler, B. Deutsch, R. Quidant, and L. Novotny, Subkelvin parametric feedback cooling of a laser-trapped nanoparticle, Phys. Rev. Lett. **109**, 103603 (2012).

[48] A. Grimm, N. E. Frattini, S. Puri, S. O. Mundhada, S. Touzard, M. Mirrahimi, S. M. Girvin, S. Shankar, and M. H. Devoret, Stabilization and operation of a Kerr-cat qubit, Nature (London) **584**, 205 (2020).

[49] Z. Wang, M. Pechal, E. A. Wollack, P. Arrangoiz-Arriola, M. Gao, N. R. Lee, and A. H. Safavi-Naeini, Quantum dynamics of a few-photon parametric oscillator, Phys. Rev. X **9**, 021049 (2019).

[50] T. Yamaji, S. Kagami, A. Yamaguchi, T. Satoh, K. Koshino, H. Goto, Z. R. Lin, Y. Nakamura, and T. Yamamoto, Spectroscopic observation of the crossover from a classical duffing oscillator to a kerr parametric oscillator, Phys. Rev. A **105**, 023519 (2022).

[51] A. Eichler and O. Zilberberg, *Classical and Quantum Parametric Phenomena* (Oxford University Press, Oxford, 2023).

[52] Note that H_{rot} may not have dimensions of energy in this notation because u and v have the same units. The quasi-Hamiltonian can be expressed in units of energy by changing $H_{\mathrm{rot}} \rightarrow H_{\mathrm{rot}}/m\omega_{\mathrm{r}}$ in Eqs. (3) and (4).

[53] A. Eichler, J. Moser, J. Chaste, M. Zdrojek, I. Wilson-Rae, and A. Bachtold, Nonlinear damping in mechanical resonators made from carbon nanotubes and graphene, Nat. Nanotechnol. **6**, 339 (2011).

[54] J. Güttinger, A. Noury, P. Weber, A. M. Eriksson, C. Lagoin, J. Moser, C. Eichler, A. Wallraff, A. Isacsson, and A. Bachtold, Energy-dependent path of dissipation in nanomechanical resonators, Nat. Nanotechnol. **12**, 631 (2017).

[55] The measurement sampling rate directly impacts the phase-space resolution. From this point of view, using the largest available sampling rate is often desirable, though this comes at the expense of large data files and increased measurement noise. If needed, data points can be averaged in post-processing to reduce noise.

[56] M. C. Lifshitz, R. Cross, Nonlinear dynamics of nanomechanical and micromechanical resonators, *Reviews of Nonlinear Dynamics and Complexity* (Wiley, New York, 2009), pp. 1–52.

[57] M. Dykman, *Fluctuating Nonlinear Oscillators* (Oxford University Press, Oxford, 2012).

[58] M.-S. Heo, Y. Kim, K. Kim, G. Moon, J. Lee, H.-R. Noh, M. I. Dykman, and W. Jhe, Ideal mean-field transition in a modulated cold atom system, Phys. Rev. E **82**, 031134 (2010).

[59] R. Karabalin, S. Masmanidis, and M. Roukes, Efficient parametric amplification in high and very high frequency piezoelectric nanoelectromechanical systems, Appl. Phys. Lett. **97**, 183101 (2010).

[60] P. A. M. Dirac, Relativistic quantum mechanics, Proc. R. Soc. London A **136**, 453 (1932).

[61] M. Soriente, T. Donner, R. Chitra, and O. Zilberberg, Dissipation-induced anomalous multicritical phenomena, Phys. Rev. Lett. **120**, 183603 (2018).

[62] G. Villa, J. del Pino, V. Dumont, G. Rastelli, M. Michałek, A. Eichler, and O. Zilberberg, Topological classification of driven-dissipative nonlinear systems, arXiv:2406.16591.

[63] L. Catalini, Y. Tsaturyan, and A. Schliesser, Soft-clamped phononic dimers for mechanical sensing and transduction, Phys. Rev. Appl. **14**, 014041 (2020).

[64] H. J. Ricardo, *A Modern Introduction to Differential Equations*, 3rd. ed., edited by H. J. Ricardo (Academic Press, New York, 2021), pp. 361–420.

[65] J. Košata, J. del Pino, T. L. Heugel, and O. Zilberberg, HarmonicBalance.jl: A Julia suite for nonlinear dynamics using harmonic balance, SciPost Phys. Codebases 6 (2022).

[66] V. Borovik, P. Breiding, J. del Pino, M. Michałek, and O. Zilberberg, Khovanskii bases for semimixed systems of polynomial equations–approximating stationary nonlinear newtonian dynamics, J. Math. Pures Appl. **182**, 195 (2024).

[67] J. Fan and S. Jia, Collective dynamics of the unbalanced three-level Dicke model, Phys. Rev. A **107**, 033711 (2023).

[68] M.-w. Xiao, Theory of transformation for the diagonalization of quadratic Hamiltonians, arXiv:0908.0787.